

# **Optimization of Weldox - SiC Armor for Ballistic Impact**



By

**Hamza Saleem Khan**

(Registration No: 00000318964)

Thesis Supervisor: Dr. Hasan Aftab Saeed

Department Of Mechanical Engineering

College of Electrical & Mechanical Engineering (CEME)


National University Of Sciences and Technology (NUST)


Islamabad, Pakistan

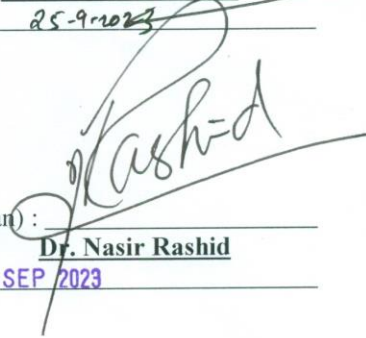
(2023)

**THESIS ACCEPTANCE CERTIFICATE**

Certified that final copy of MS thesis written by Ms. **NS Hamza Saleem Khan**, Registration No. **00000318964** of **NUST College of E&ME** has been vetted by undersigned, found complete in all respects as per NUST Statutes/Regulations, is free of plagiarism, errors, and mistakes and is accepted as partial fulfillment for award of MS degree. It is further certified that necessary amendments as pointed out by GEC members of the scholar have also been incorporated in the said thesis.

Signature:   
Name of Supervisor: **Dr. Hasan Aftab Saeed**  
Date: 25-09-2023

Signature (HOD):   
Name: **Dr. Imran Akhtar**  
Date: 25-9-2023

Signature (Dean):   
Name: **Dr. Nasir Rashid**  
Dated: 25 SEP 2023

# **Optimization of Weldox - SiC Armor for Ballistic Impact**

By

**Hamza Saleem Khan**

**(00000318964)**

A Thesis

Of

Master of Science

Submitted to

**Department Of Mechanical Engineering**

**College of Electrical & Mechanical Engineering (CEME)**

**National University Of Sciences and Technology (NUST)**

**Islamabad, Pakistan**

In partial fulfillment of the requirements for the degree of

**Master of Science Mechanical Engineering**

**September, 2023**

## **Dedication**

*Dedicated to my exceptional parents and caring brother  
whose tremendous support and cooperation led me to this  
wonderful achievement*

## **ACKNOWLEDGEMENTS**

I extend my heartfelt gratitude to:

Almighty Allah: For granting me the wisdom, strength, and perseverance throughout this academic journey.

My Parents: Your unwavering support, encouragement, and sacrifices have been the cornerstone of my success. Your love has been my driving force.

Dr. Hasan Aftab Saeed: I am indebted to you for your guidance, expertise, and constant encouragement. Your insights and mentorship have been invaluable in shaping this thesis.

Dr. Naveed Akmal Din: Your insightful feedback and constructive criticism have significantly enriched the quality of my work. Your contributions are deeply appreciated.

Prof. Yasser Riaz Awan: I extend my gratitude for your valuable input and thoughtful suggestions, which have greatly contributed to the refinement of this thesis.

I am truly fortunate to have been surrounded by such incredible individuals who have played pivotal roles in my academic journey. Thank you for your unwavering support, guidance, and belief in my abilities.

## **ABSTRACT**

In recent times, the armor industry has experienced substantial growth, accompanied by significant financial investments aimed at developing and testing new armor solutions. Conducting ballistic studies through experimental setups incurs high costs and involves intricate procedures, incorporating numerous sensors and advanced imaging technology. Despite the reliability of experimental data, it often falls short of capturing all essential parameters. Consequently, extensive research is underway to formulate numerical and analytical models that can precisely predict the ballistic performance of novel armor materials and designs.

This thesis undertakes an exploration of the ballistic behavior of both monolithic and multi-layered target sheets against blunt projectiles. Various impact phenomena, including Adiabatic Shear Localization, Thermal Plastic Instabilities, and high stress gradients, have been modeled utilizing an explicit analysis solver based on the Finite Element Method (FEM). This involves the use of appropriate strength, failure, and shockwave models for both brittle and ductile materials. The chosen target configurations were subjected to testing against blunt projectiles traveling at velocities ranging from 100 to 500 m/s. The results of impact simulations have been carefully compared with experimental data.

The thesis delves into the ballistic performance of multilayered targets constructed from different combinations of materials such as Weldox 460E, Al 7075 T6, and SiC, each with varying thicknesses. Furthermore, the prevalent failure modes in each case were observed and identified. The study demonstrates that FEM-based simulations, employing meticulously chosen material properties and computational models, yield highly comparable outcomes to experimental data. Ultimately, the thesis presents a comprehensive analysis of three distinct multi-layered target configurations composed of different materials, when subjected to the impact of a blunt projectile.

# TABLE OF CONTENTS

<b>ACKNOWLEDGEMENTS .....</b>	<b>v</b>
<b>ABSTRACT .....</b>	<b>vi</b>
<b>TABLE OF CONTENTS .....</b>	<b>vii</b>
<b>LIST OF FIGURES.....</b>	<b>ix</b>
<b>LIST OF TABLES.....</b>	<b>x</b>
<b>CHAPTER 1: INTRODUCTION.....</b>	<b>1</b>
1.1 Motivation.....	1
1.2 Impact Mechanics .....	1
1.3 Low Ductility .....	3
1.4 High Ductility .....	4
1.5 Ballistic Testing Standard .....	6
<b>CHAPTER 2: LITERATURE REVIEW .....</b>	<b>7</b>
2.1 Monolithic Metallic Sheets .....	7
2.2 Multilayered Metallic Sheets .....	8
2.3 Multilayered Sandwich Core with Ceramic Plates.....	10
2.4 Promising Materials .....	11
<b>CHAPTER 3: COMPUTATIONAL MODELING.....</b>	<b>13</b>
3.1 Lagrangian Formulation.....	13
3.2 Eulerian Formulation .....	14
3.3 Arbitrary Lagrangian - Eulerian Formulation .....	14
3.4 Smooth Particle Hydrodynamics.....	14
3.5 SFM.....	15
3.6 Johnson and Cook Strength Model .....	16
3.6.1 Modeling Parameters .....	16
3.7 Johnson Holmquist Strength Model.....	17
3.7.1 Strength Model .....	18
3.7.2 Damage Model.....	18
3.8 Shock Wave Formation and Equation of State.....	19
3.8.1 Rankine Hugoniot Relations .....	20
3.8.2 Gruneisen EOS .....	20
3.8.3 Polynomial EOS .....	21
3.9 Failure Model.....	21
3.9.1 Triaxial Stress State ( <b>D1, D2, &amp; D3</b> ) .....	22
3.9.2 High Strain Rate Stress State ( <b>D4</b> ) .....	23
3.9.3 High Temperature Environment ( <b>D5</b> ).....	23
<b>CHAPTER 4: ANALYTICAL MODELING .....</b>	<b>24</b>
4.1 Localized Interaction Approach.....	24
4.2 Cavity Expansion Approximation .....	25

4.3	Lambert-Jonas Approximation.....	25
4.4	Commonly Used Analytical Models and Their Application .....	26
<b>CHAPTER 5: NUMERICAL SETUP.....</b>		<b>28</b>
5.1	Simulation Parameters .....	28
5.2	Mesh Independence Study .....	30
5.3	Material Properties .....	31
<b>CHAPTER 6: NUMERICAL RESULTS .....</b>		<b>33</b>
6.1	Blunt Projectiles against Monolithic Sheet .....	33
6.1.1	Weldox 460E .....	33
6.1.2	Al 7075 T6.....	35
6.1.3	Silicon Carbide .....	36
6.2	Multi-Layered Targets .....	38
6.2.1	Weldox 460E – SiC .....	38
6.2.2	Al 7075 T6 – SiC .....	41
6.2.3	Weldox 460E – Al 7075 T6.....	43
6.3	Results Discussion: .....	45
<b>Chapter 7: CONCLUSION.....</b>		<b>47</b>
<b>Chapter 8: FUTURE WORK .....</b>		<b>48</b>
<b>REFERENCES .....</b>		<b>49</b>



## LIST OF FIGURES

Figure 1-1: Common Failure Modes.....	3
Figure 1-2: Ballistic Limit Curve.....	5
Figure 2-1: Sandwich Panels .....	11
Figure 3-1: Von-Mises Equivalent Stress versus Pressure in JH-1(Left) and JH-2 (Right)....	18
Figure 5-1: Dimensions of Blunt Faced Projectiles.....	28
Figure 5-2: Mesh of Blunt Projectile and Target.....	29
Figure 5-3: Mesh Independence Study .....	31
Figure 6-1: Energy Comparison.....	33
Figure 6-2: Penetration in Weldox 460E, Initial Velocity = 296m/s.....	34
Figure 6-3: Experimental [3], Analytical & Numerical Solution of Weldox 460E.....	34
Figure 6-4: Penetration in Al 7075 T6, Initial Velocity = 400m/s.....	35
Figure 6-5: Comparison of Experimental & Numerical Solution Al 7075 T6 .....	36
Figure 6-6: Crack Propagation in SiC.....	36
Figure 6-7: Stress Wave Propagation Conoid in SiC.....	37
Figure 6-8: Penetration in Weldox 460E - SiC, Initial Velocity = 296m/s.....	38
Figure 6-9: Ballistic Curve for Combination of 6mm Weldox 460E and 3mm SiC .....	40
Figure 6-10: Penetration in Al 7075 T6 - SiC, Initial Velocity = 296m/s .....	41
Figure 6-11: Ballistic Curve for Combination of 13mm Al 7075 T6 and 2mm SiC.....	42
Figure 6-12: Penetration in Weldox 460E - Al 7075 T6, Initial Velocity = 296m/s .....	43
Figure 6-13: Ballistic Curve for Combination of 5mm Weldox 460E and 3mm Al 7075 T6.....	44

## LIST OF TABLES

Table 0-1: Mesh Independence Study.....	30
Table 6-1: Residual Velocity for Varying Thickness of Weldox 460E - SiC, Initial Velocity = 296m/s.....	39
Table 6-2: Residual Velocity for Varying Thickness of Weldox 460E – SiC, Initial Velocity = 161.2m/s.....	39
Table 6-3: Weight (kg) for Varying Thickness of Weldox 460E – SiC .....	39
Table 6-4: Residual Velocity for Varying Thickness of Al 7075 T6 – SiC, Initial Velocity = 296m/s.....	41
Table 6-5: Weight (kg) for Varying Thickness of Al 7075 T6 – SiC.....	42
Table 6-6: Residual Velocity for Varying Thickness of Weldox 460E - Al 7075 T6, Initial Velocity = 296m/s.....	43
Table 6-7: Weight (kg) for Varying Thickness of Weldox 460E - Al 7075 T6 .....	44
Table 6-8: Comparison of Different Target Configurations .....	45

# CHAPTER 1: INTRODUCTION

## 1.1 Motivation

Throughout human history, acts of violence such as warfare and criminal acts involving bombings and killings have been deeply ingrained in society. Humans have consistently sought ways to prepare for such events by constructing fortified structures like castles, bunkers, and subterranean abodes. The safety and safeguarding of individuals have always remained paramount. Over the course of time, advancements in weaponry have drastically enhanced, enabling precise targeting even at substantial distances. In contrast, the development of armor was largely overlooked until the onset of the First World War, when traditional techniques and materials persisted. The escalating velocity and caliber of bullets necessitated a comprehensive overhaul of armor methods.

Recognizing this need, contemporary materials are presently being engineered with the primary aim of shielding against ballistic impacts. Beyond bullets, the shrapnel generated by roadside bombings and suicide attacks contributes significantly to fatalities. Consequently, security forces necessitate superior protective gear to counter these emerging forms of terrorist threats. However, it's not solely armed and paramilitary forces facing jeopardy from firearm assaults. Government officials and public figures also require safeguards against unforeseen dangers.

Analyzing statistical data reveals that a substantial 80-90% of terrorist incidents transpire while victims are in transit via automobiles. This grim reality has resulted in the loss of numerous security personnel's lives due to suicide bombers and improvised explosive devices (IEDs). Given the current national context, accessible security solutions are imperative. Adequately armored vehicles, whether manned or unmanned, have the potential to effectively neutralize potential terrorists and offer essential security during troop movements and patrols, guarding against unforeseen eventualities.

Researchers dedicated to the study of impact dynamics hold a pivotal role in advancing these objectives.

## 1.2 Impact Mechanics

Extensive research within the field of impact dynamics has yielded a substantial body of literature. A significant portion of these studies has been conducted on generic components under ideal impact scenarios, involving the normal collision of moving projectiles on

stationary targets. However, it's important to note that these idealized conditions are primarily feasible within controlled laboratory settings. In real-world applications, a wide array of projectile-target combinations exists, often differing considerably from the standardized scenarios explored in laboratory investigations.

Structural impact dynamics exhibit distinct characteristics that set them apart from traditional quasi-static loading conditions. From a physical perspective, the consideration of inertia effects becomes crucial in governing equations. This leads to stress waves within both the impacting projectile and the target, underscoring the acknowledgment that transient impact events deviate from steady-state conditions. Additionally, the abbreviated duration of impact occurrences introduces strain effects, thermal softening, and hydrodynamic material behavior, phenomena rarely encountered in quasi-statically loaded materials. Furthermore, tackling the challenges of the high-rate loading associated with impact dynamics is demanding, encompassing difficulties in applying the load and recording the response.

Impact dynamics stands out due to two key elements that distinguish it from classical mechanics applied to deformable or rigid bodies under quasi-static conditions. First feature pertains to the propagation of stress wave in analysis of the problem, highlighting that most of the impact events are transient occurrences devoid of steady-state equilibrium [1]. Second aspect entails the prominence of inertia effects, necessitating their consideration in equations rooted in the laws of conservation.

In addressing impact problems, three fundamental approaches are commonly employed. The empirical approach relies on experimental data and, with suitable equipment and setups, yields highly accurate outcomes. Despite its realism, extrapolating results specific to particular problems can be challenging. The second approach involves the formulation of ballistic impact models founded on momentum and energy conservation principles. These models incorporate material properties such as density, yield strength, and ultimate tensile strength. However, certain models, like Lambert and Jonas' proposals, rely heavily on curve-fitting techniques, often tailored to specific problems or material sets. The third approach entails discretization, utilizing either Lagrangian or Eulerian schemes. The accuracy of the solution obtained depends on the adopted failure and strength models, albeit at the cost of increased computational time. Precision can be enhanced by selecting appropriate modeling parameters and techniques.

Numerous publications in this domain have resulted in the inconsistent use of technical terms, potentially causing confusion due to their ambiguous meanings. To clarify, in contemporary science, Ballistics pertains to the study of the impact of projectiles, particularly the ones fired

from guns. Throughout our work, our primary focus will center on investigating terminal ballistics, which encompasses the interaction between projectiles and targets during impact. This area holds particular significance in the context of armoring, defined as structures employed to enhance strength, especially in military defenses. During an impact event, projectiles can penetrate targets in various ways. According to Backman and Goldsmith (1978), these methods can be categorized as follows:

- a. Perforation: The projectile traverses the target, retaining residual velocity upon passage.
- b. Ricochet: The projectile gets deflected away from the target without coming to a halt.

Figure 1 illustrates the prevalent failure modes observed when projectile strength surpasses target strength. These failure modes are grouped into two overarching types based on the ductility of the target material.

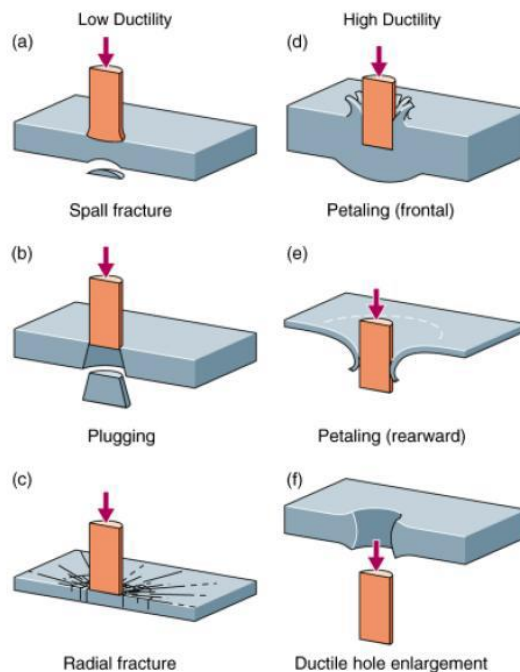


**Figure 1-1: Common Failure Modes**

### 1.3 Low Ductility

Within the low ductility regime, further categorization has been established encompassing three distinct failure modes, contingent upon factors like target material, thickness, and strength:

- a. Spall fracture (Fig-1(a)): This form of fracture is typically evident on the back side of the target. A compressive shock wave, originating from the impact point, is reflected as a tensile wave from the opposite end of the target. The occurrence of target failure via spall

fracture arises when the magnitude of the reflected tensile wave is larger than the tensile strength of the material.

- b. **Plugging (Fig-1(b)):** This failure mechanism tends to manifest in highly ductile metallic targets. An ejected plug, roughly equivalent in diameter to the projectile, emerges from the targets back side. This outcome is attributed to the formation of intense stress shear zones surrounding the circumferential periphery of the moving projectile. The temperature within these shear zones often approaches the material's melting point. In the context of metals, this phenomenon is commonly referred to as Adiabatic shearing.
- c. **Radial fracture (Fig-1(c)):** This failure mode is prevalent among ceramic targets, primarily due to ceramics having a lower tensile strength in comparison to their compressive strength. The same compressive stress wave observed in the impact of ductile materials triggers radial tensile stresses in this instance, resulting in radial fracture.

## **1.4 High Ductility**

Within the high ductility regime, a broad classification into two failure modes exists, contingent upon target thickness. This classification encompasses highly ductile materials such as stainless steel and polymers:

- a. **Petaling (Figs-1(d) and (e)):** Two distinct types of petaling can be observed: Frontal (Fig-1(d)) and Rear (Fig-1(e)). Frontal petaling is the predominant mode of failure in soft, ductile targets impacted by sharp projectiles. This is attributed to the presence of exceedingly high tensile stress as the initial stress wave traverses the target. Within the critical area of penetration, both radial and circumferential tensile stresses emerge. Notable plastic deformation becomes apparent as the target material flows ahead of the impacting projectile. A petal-like shape forms in front of the projectile due to the radial expansion of the initial hole, generated by the material flow following projectile impact. As the target thickness decreases, the work necessary for target bending and stretching diminishes in contrast to radial expansion. Consequently, the high bending stresses resulting from projectile impact lead to rear petaling, a failure mode also known as dishing.
- b. **Ductile Hole Enlargement (Fig-1(f)):** This type of failure is frequently observed in relatively thick targets subjected to impact of projectiles with sharp-nose, including ogival and conical variants. Upon projectile impact, the kinetic energy of the projectile displaces adjacent target material, creating a hole within the target plate. As the projectile

penetrates the target, the radius of the initial hole expands. Both plugging and ductile hole enlargement represent similar failure modes wherein projectile kinetic energy transforms into plastic deformation. However, ductile hole enlargement gains prominence when the target thickness surpasses the diameter of projectile.

Ballistic limit velocity represents the average between the maximum velocity of the projectile that fails to penetrate the target and the minimum velocity of the projectile that results in complete target penetration. In conjunction with this, the ballistic limit curve serves as a crucial metric within structural impact analysis. This curve depicts the residual velocity of the projectile as a function of the initial velocity of the projectile.

When residual velocity is plotted against impact velocity, it generates graphs commonly referred to as "Ballistic limit curves." These curves provide a reliable means to assess a target's ballistic resistance and its performance under varying projectile impact velocities. The presented plots offer a comprehensive overview of the penetration capability of blunt projectiles against targets of differing thickness.

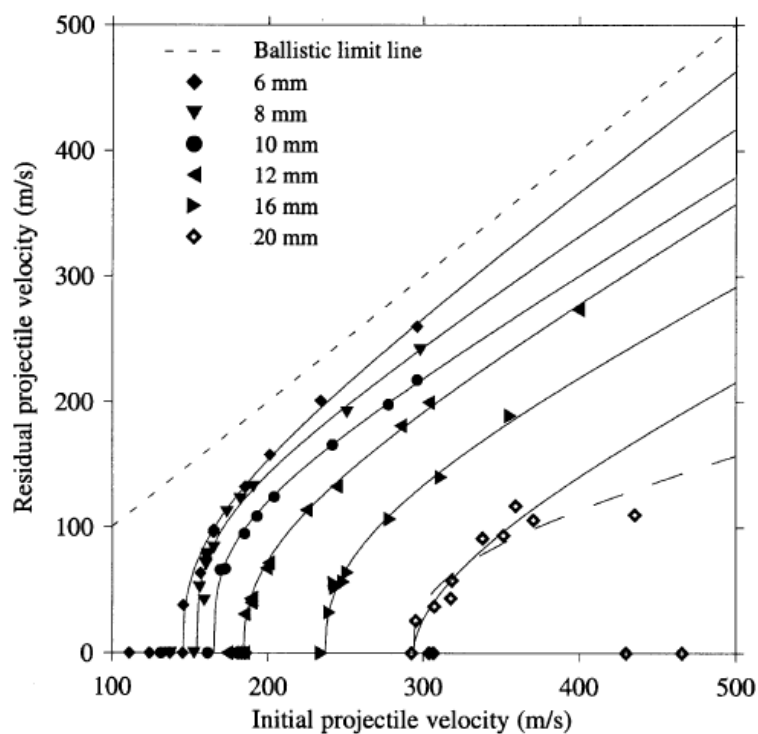


**Figure 1-2: Ballistic Limit Curve**

Experimental investigations into ballistics can be broadly categorized into three primary groups depending on the projectile's impact velocity. The first group encompasses projectiles with impact velocities below 50 m/s, applicable to heavy projectiles employed with methods like drop hammers or pneumatic accelerators. The second group pertains to projectiles with

sub-ordnance to ordnance velocities, which are typically accelerated using compressed gas guns to attain impact velocities in the range of 50 to 1300 m/s. Majority of the research conducted in this study focuses on this range of impact velocities. The final category involves projectiles in the hyper-velocity section, achieved through the utilization of light gas guns with two-stages and low-mass projectiles.

This research study primarily concentrates on the sub-ordnance velocity regime, with a small number of simulations conducted within the ordnance velocity section. The overarching objective of this thesis is to determine an optimal armor solution while simultaneously validating the outcomes of ballistic experiments through an integrated approach involving numerical and analytical methods.

## **1.5 Ballistic Testing Standard**

The primary goal underlying the investigation of ballistic impact phenomena is to enhance the efficiency of current protection methodologies. However, it's important to recognize that such protection cannot be universally effective against all types of projectiles. Consequently, the scope of our study must be confined by considering the specific projectile characteristics and velocities under investigation.

In this endeavor, we will simplify the geometries of the objects involved to ensure the validation of our simulation setup and methodologies. It is worth noting that many research teams have initiated their studies using blunt, ogival, or conical-shaped projectiles as initial benchmarks. The eventual determination of the optimal armor solution hinges upon its demonstrated ballistic resistance against blunt projectiles, characterized by initial impact velocities ranging between 200 and 600 m/s. This targeted approach allows us to effectively assess the protective capabilities of different materials and designs under realistic conditions.



## CHAPTER 2: LITERATURE REVIEW

The majority of research conducted by military and industrial research organizations within the realm of armor development is often not readily accessible to the general public. Nonetheless, a substantial amount of experimental data is accessible through published literature originating from research laboratories worldwide. The objectives of these research studies encompass a wide spectrum, spanning from investigating the influence of diverse projectile shapes to analyzing the ballistic resilience of distinct target materials across varying thicknesses.

### 2.1 Monolithic Metallic Sheets

Borvik et al. [3,4] were pioneers in thoroughly investigating the ballistic resistance characteristics of monolithic sheets. Their research extensively relied on experimental investigations. They conducted comparative analyses of analytical and numerical outcomes for steel targets of Weldox 460 E in terms of ballistic resistance. The variables examined during their tests included plate thickness in range of 6 to 30 mm, projectile nose shape (blunt, conical), and initial projectile velocity. Their findings demonstrated that the target's reaction becomes particularly responsive to alterations in impact velocity when approaching the vicinity of the ballistic limit velocity. Furthermore, they demonstrated that the ballistic limit curve exhibits a sudden transition to zero residual velocity at the exact ballistic limit velocity, devoid of preceding indications. They introduced a hypothetical line termed the ballistic limit line onto their plots, representing the ballistic limit velocity of a target with zero thickness. Borvik et al. also noted that the plug velocity exceeds the projectile's residual velocity.

Borvik's study delved into the kinetic energy absorbed as the projectile endeavors to penetrate the target. The findings revealed that this absorbed kinetic energy stabilizes with increasing impact velocity. Concurrently, target deformation diminishes as impact velocity escalates. Conversely, with decreasing impact velocity, deformation increases up to a maximum until the ballistic limit velocity is reached. This deformation can be classified into two forms: local and global. Global deformation heightens as impact velocity decreases, whereas local deformation follows the opposite trend, increasing with impact velocity. Notably, there exists an upward trajectory in the plastic deformation of the projectile as the projectile velocity rises.

Another significant facet of ballistic studies pertains to the failure mechanisms of targets, as introduced in the Introduction. The failure of a target hinges on a range of factors including projectile shape, material properties, target thickness and velocity. Backman and Goldsmith summarize these penetration mechanisms, including radial fracture resulting from initial stress waves in brittle materials, compressive stress wave failure, ductile hole enlargement, and plugging. Among these, plugging and ductile hole enlargement stand out as the predominant failure modes for metallic targets.

A closer examination of plugging and ductile hole enlargement underscores their distinct energy absorption characteristics. Plugging, through the adiabatic shear phenomenon, generates high shear stress regions around the projectile's edges. Conversely, the process of ductile hole enlargement propels material ahead of the projectile, demanding more energy compared to plugging. For relatively thin targets, plugging involves localized shear and global bending. In thick targets, initial perforation may involve ductile hole enlargement, but as the target thickness in front of the penetrating projectile decreases, the mechanism shifts to plugging, which dissipates impact energy more rapidly. Microscopic analysis by T. Borvik et al. of perforated target sheets revealed heavily deformed shear bands in 10–16 mm thick targets, along with observations of transformed adiabatic shear bands in targets with relatively large thickness.

## **2.2 Multilayered Metallic Sheets**

The inquiry into multi-layered targets prompted initial questions concerning whether there were advantages in dividing a monolithic target, such as a 10 mm thick Weldox sheet, into two 5 mm plates. Additionally, there was a debate between using spaced plates versus layered ones. Marom and Bonder adopted a combined analytical and experimental approach, utilizing a spherical nose projectile to address these concerns. They deduced that monolithic targets exhibited higher ballistic resistance compared to multi-layered targets when the sheets were joined without any spacing. However, the inverse held true for spaced shields.

However, these findings, while seemingly conclusive, were met with challenges from other researchers in the ballistic field. Radin and Goldsmith contradicted these results when examining blunt and conical projectiles against multi-layered shields with thicknesses ranging from 1.6 to 6.4 mm. Their experimental findings demonstrated that monolithic targets outperformed multi-layered ones against all types of projectiles. Almohandes et al. corroborated these conclusions through a comprehensive experimental study on 7.62 mm bullets. They explored three target configurations: spaced, layered, and monolithic, with

thicknesses varying from 8 to 14 mm. Their results aligned completely with those of Radin & Goldsmith. They also determined that the difference in ballistic resistance between monolithic and layered targets decreased with increasing impact velocity. Furthermore, Alomohandes et al. found that within a double-layered target, a thicker rear plate resulted in greater ballistic resistance compared to a thin rear plate. As for multi-layered targets, an increase in the number of layers led to a decline in ballistic resistance. They also discovered that multi-layered plates filled with polyester exhibited higher ballistic resistance than steel targets of equivalent weight.

Liang et al. [2005] introduced an approximate penetration model, which they validated using the experimental findings of Almohandes et al. [1996]. They suggested an optimum ratio of the front plate's thickness to overall thickness of the target based on their analytical model. The best outcomes were achieved with a thickness ratio of 0.75, while the minimum ballistic resistance was observed for a thickness ratio of 0.5. They also investigated the impact of an air gap situated between two plates within double-layered targets.

Dey et al. conducted a thorough numerical and experimental analysis of multi-layered steel targets. They noted that the ballistic limit velocity of a double-layered target exceeded that of a monolithic target by 30% when dealing with blunt-nose projectiles. Despite the abundance of research data available, experimental analyses have sometimes yielded contradictory findings for the same projectile-target impact configurations.

Corran et al. concluded that a double-layered target might yield a higher ballistic limit velocity if the target thickness exceeded a certain value. They plotted penetration energy against target thickness for somewhat hemispherical projectiles and noted a sharp inflection in the curve at a value of 3.5 mm. Below this threshold, multi-layered targets did not confer any benefits, attributed to a change in energy absorption methods. Corren et al. also determined that the order of sheets in a target with uneven sheet thickness was crucial. Additionally, they calculated that the best combination of front and rear sheet thicknesses, both above 3.5 mm, could yield results comparable to monolithic targets.

Nixdorff's work suggested that partitioning a monolithic and homogeneous target into multiple layers resulted in a decrease in the target's ballistic limit velocity, drawing from a theory published by Awerbuch and Bodner.

Zukas and Scheffler conducted an extensive numerical study of metallic targets. They introduced a parameter  $b/2R$ , where  $b$  and  $R$  are the target thickness and the radius of the projectile's shank, respectively. They concluded that layering had a significantly negative effect on the ballistic properties of thin ( $b/2R < 1$ ) and intermediate thickness ( $3 < b/2R < 10$ )

targets. Moreover, for thick targets where ( $b/2R > 10$ ), layering did not significantly alter the residual properties of the projectile compared to monolithic equivalents.

Madhu et al. conducted extensive experimental work on normal impacts of aluminum targets and compared monolithic targets with double and triple-layered plates of equal thickness. They found that layering did not enhance the ballistic resistance of intermediate thickness targets. Their results for steel and aluminum targets aligned with the findings of Zukas & Scheffler, and these findings can be extrapolated to other metallic targets.

While steel is a high-density material, its superior ballistic performance can sometimes be overshadowed. Considerable research, predominantly based on numerical and analytical results, has explored the impact of various metallic combinations in multi-layered targets. Zukas also proposed an analytical solution regarding the arrangement of metallic sheets of different materials in a multi-layered target. Their objective was to optimize the synergistic impact of ductility and strength to enhance energy dissipation and suggested that metallic layers should be ordered based on increasing values of the parameter  $x$ , which is the ratio of dynamical hardness to density. This arrangement positioned aluminum ahead of steel for better ballistic performance. Another novel proposal involves substituting some of the steel mass from the target with relatively less dense ceramic plates with high compressive strength.

### **2.3 Multilayered Sandwich Core with Ceramic Plates**

A recent development in the realm of multi-layered targets involves the use of a double-layered target with a sandwich core. This core is filled with an optimal material, typically ceramic or polymer, to enhance ballistic performance. The concept is to replace high-density steel with lightweight alternatives without compromising ballistic effectiveness. Alternatives like ceramics not only reduce target weight but also possess unique ballistic resistance properties, such as the interface defeat phenomenon. This property causes ceramics to deform the projectile, effectively dissipating a significant portion of its kinetic energy. Mushrooming, characterized by plastic deformation, is a common outcome when projectiles impact ceramic targets. Placing this ceramic plate between two metallic plates further pulverizes it, reducing the kinetic energy of the penetrating projectile.

Sarva et al. proposed that the ballistic efficiency can be enhanced by up to 25% with just a 2.5% increase in areal density by sandwiching a ceramic tile between two ductile plates. This confinement on both sides results in an increase in the strength of ceramics, as noted by Deshpande and Evans. The remarkable improvement in ceramic's ballistic performance is attributed to a change in the failure mode. The figure below illustrates the variation in the

failure mode. Even after pulverization, ceramics continue to bear a significant portion of the impact force.

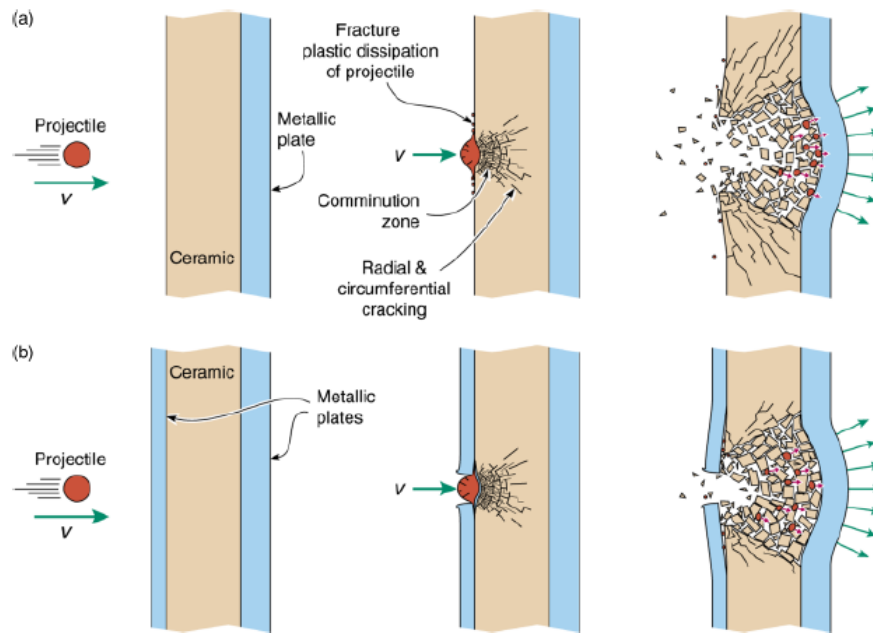


**Figure 2-1: Sandwich Panels**

Christian et al. investigated a stainless steel sandwich structure featuring a pyramidal-shaped truss core filled with polyurethane and alumina when faced with a spherical projectile. Their findings indicated that the inclusion of a polyurethane core did not enhance the ballistic limit beyond that of a monolithic steel target. However, it did lead to a reduction in the projectile's kinetic energy. This outcome is attributed to the failure of polyurethane caused by hole enlargement, which inadequately disperses the impact load. On the other hand, targets with alumina inserts performed well by eroding the impacting projectile while simultaneously engaging the steel plates to absorb impact energy. This innovative approach signifies a promising avenue for enhancing the efficiency of multi-layered targets while exploring alternative materials and configurations.

## 2.4 Promising Materials

Plastic deformation in metals primarily converts into heat, particularly when it cannot dissipate efficiently due to high-speed deformation. This often results in a rise in temperature, especially in cases of metals where the rate of thermal softening surpasses the rate of work hardening. In such instances, deformation tends to concentrate in a narrow softened region, generating a band of adiabatic shear [1]. The process of ballistic penetration triggers localized phenomena that induce shock waves, causing exceptionally high strain rates contingent upon

the velocity of the impacting projectile. Adiabatic shear is a deformation mode unique to these high strain rates. When metals undergo ballistic penetration, they experience substantial plastic deformation, with about 95% of this deformation being converted into heat, leading to temperature elevation. Adiabatic deformation necessitates low thermal conductivity and a brief deformation time, rendering it a crucial phenomenon to model in scenarios involving high-velocity impact loading.

Yellup and Woodward [5] formulated a graph ranking materials based on their strength-to-weight ratio and their susceptibility to adiabatic shear. Their analysis revealed that adiabatic deformation demands materials with low thermal conductivity and extremely short deformation times, often on the order of milliseconds to microseconds. Selecting an optimal material with the appropriate properties is a pivotal factor in achieving high ballistic resistance. In this context, ceramics play a significant role. The combination of ceramics' high strength and low density allows for the design of weight-efficient armor systems with substantial protective capabilities. A wide range of options are available, spanning from metallic shields like steel and aluminum to composites such as SiC and Boron Carbide. Each material possesses distinct properties like density, yield strength, and specific heat. Carbides, for instance, exhibit high compressive strength relative to their tensile strength, making them advantageous during projectile penetration. However, the optimum material selection doesn't hinge on a single metallic or non-metallic sheet; rather, it relies on the astute combination of different materials to achieve the desired protective outcome.

## CHAPTER 3: COMPUTATIONAL MODELING

The interaction between a projectile and its target involves the transfer of kinetic energy through a process akin to fluid flow. When the projectile impacts the target, it endeavors to create a pathway within the target, similar to how fluid flows through a narrow passage. The loss of material in projectile impact situations is primarily attributed to erosion. In the course of this erosion, shock waves are generated and propagate outward from the points of contact. Concurrently, release waves originating from the boundaries of the projectile induce lateral movement in both the projectile and target materials.

A solid material experiencing deformation at an arbitrary rate can respond through six fundamental mechanisms: Phase Changes, Homogeneous Plastic Flow, Elastic Distortion, Formation and expansion of ductile micro voids, Creation and enlargement of brittle micro cracks, and shear instabilities initiation and growth [8]. Given the resource-intensive and intricate nature of experimental studies involving impact, it becomes essential to have a reliable and efficient computational approach. Established software packages such as ABAQUS, AutoDyn, and LS Dyna have been developed to address these transient loading scenarios. However, the challenge lies in accurately representing a diverse range of materials, spanning from ductile to brittle substances. To achieve a faithful simulation of projectile impact, a pragmatic strategy is necessary, encompassing complex phenomena like High Stress Gradients, Thermal Plastic Instabilities and Adiabatic Shear Localization. The dynamics of deformation processes are typically captured through the decomposition of the stress tensor. This decomposition yields the Deviatoric stress tensor  $\sigma_{ij}^D$  and the Spherical hydrostat  $\sigma_H \delta_{ij}$ , which correspond to plasticity and pressure components, respectively.

$$\sigma_{ij} = \sigma_{ij}^D + \sigma_H \delta_{ij} \quad \rightarrow (1)$$

In the realm of numerical methodologies for solving such impact-related problems, five main approaches are commonly employed: Smooth Particle Hydrodynamics (SPH), Arbitrary Lagrangian Eulerian (ALE), Lagrangian, Eulerian, and SFM models. The latter two methods can be categorized as extensions of Mesh-Free techniques.

### 3.1 Lagrangian Formulation

Within the framework of Lagrangian formulation, every discrete node of the mesh traces the trajectory of the corresponding material particle as it moves. These codes possess a clear conceptual structure and effectively manage boundary conditions at open and interacting

interfaces separating diverse materials. Nevertheless, a significant drawback is their incapacity to accurately trace extensive distortions of the computational domain unless frequent remeshing procedures are employed.

### **3.2 Eulerian Formulation**

Eulerian codes utilize a stationary grid in space, while the material continuum shifts in relation to this grid. The constituents of the grid are linked through connections between grid points, forming elements. Consequently, the Eulerian mesh must encompass a substantial expanse to effectively simulate both current and potential zones where material might propagate. Eulerian codes are adept at managing flows characterized by significant distortions. However, they inadvertently incorporate somewhat imprecise computations of free surface motion and encounter challenges in accurately representing conditions at material interfaces.

### **3.3 Arbitrary Lagrangian - Eulerian Formulation**

This technique was derived to address inherent challenges in both Eulerian and Lagrangian approaches, while harnessing their respective advantages. Within the ALE framework, computational nodes can be operated in a manner akin to conventional Lagrangian motion, held steady as in Eulerian methodology, or mobilized according to arbitrary specifications, facilitating seamless rezoning. This technique accommodates extensive deformations within the material continuum by affording flexibility in computational mesh movement, while maintaining a higher level of resolution compared to typical Eulerian methods.

In contrast to the Eulerian approach, Lagrangian codes involve fewer computations per cycle since there are no convective terms governing material motion through a grid. This characteristic simplifies the acquisition of time histories. However, the Finite Element Method (FEM) grapples with a significant issue of mesh distortion when employed in high-velocity impact analyses. This phenomenon gives rise to numerical challenges, including problem of negative volume and early termination of the analysis.

### **3.4 Smooth Particle Hydrodynamics**

The fourth technique is the Mesh-Free approach. Traditional mesh-based methods often struggle to accurately handle discontinuities that do not align with the original mesh structure. The frequent remeshing used to address shifting discontinuities can yield imprecise outcomes and require substantial computational resources. The fundamental goal of Mesh-Free



techniques is to alleviate, to some extent, this dependence on mesh by constructing approximations solely based on nodes. One widely adopted mesh-free technique is Smooth Particle Hydrodynamics (SPH).

SPH is a technique free of mesh and particularly well-suited for addressing non-linear problems characterized by substantial deformations. This method is believed to surmount the limitations of both Eulerian and Lagrangian approaches. In the SPH framework, mobile points referred to as particles, each possessing a fixed mass, establish coherence through an interpolation function. The conservation of energy, mass and momentum and is described using kernel estimations through interpolation sums. Instead of employing traditional elements, a physical entity is defined by an array of SPH points.

A notable challenge of the SPH formulation is the occurrence of significant velocity oscillations in individual particles. Moreover, standard SPH methods are associated with inherent issues like tension instability and unstable execution due to shockwaves. These concerns are often mitigated by employing a combination of corrective measures. For instance, the artificial viscosity term and additional stress method are introduced to address the respective insufficiencies [26].

### **3.5 SFM**

Similar to the ALE concept, a combined SPH-FEM approach is introduced, where SPH particles are employed in regions anticipated to undergo significant deformation and damage, while the Finite Element (FE) mesh models the remainder of the domain.

This strategy proves advantageous when SPH is confined to severely distorted sections and FEM is utilized in areas further from these zones. An approach proposed by S. Swaddiwudhipong et al. [26] combines smooth particle hydrodynamics and FEM to investigate the penetration of AA5083-H116 and Weldox 460E plates. These plates have different thicknesses and are impacted by projectiles with diverse nose geometries, including ogival, blunt and conical designs. Their study demonstrates that SFM can replicate the failure mechanisms seen in many experimental studies for projectile impact velocities of 170 m/s and higher.

When dealing with elastic-viscoplastic materials, the Cauchy stress tensor  $\sigma_{ij}$  solely relies on the strain state. The yield stress undergoes changes as plastic deformation and its rate increase beyond certain stress thresholds. Employing elasto-visco-plasticity alongside damage constitutive equations within a Finite Element numerical approach is feasible, given the accurate representation of temperature effects through appropriate functions. For the

latter, the yield stress function with respect to strain rate and temperature can be used effectively.

### 3.6 Johnson and Cook Strength Model

These scientists formulated the equivalent stress as a composite function involving temperature, strain rate and plastic strain. This model stands out due to its practicality, owing to the availability of a diverse array of tests that enable the determination of thermal, dynamic and static parameters. The multiplication of three distinct components succinctly captures the intricate interplay among strain, strain rate, and temperature in influencing stress distribution.

$$\sigma_y = [A + B\varepsilon_p^n] \left[ 1 + C \ln \left( \frac{\dot{\varepsilon}_p}{\dot{\varepsilon}_0} \right) \right] \left[ 1 - \left( \frac{T - T_r}{T_m - T_r} \right)^m \right] \rightarrow (2)$$

In the given expressions, where A represents the initial yield stress, B denotes the strain hardening coefficient, and n stands for the strain hardening exponent. The variable  $\varepsilon_p$  signifies the plastic strain rate,  $\dot{\varepsilon}_0$  corresponds to the reference strain rate, and C represents the strain rate coefficient. Additionally,  $T_r$  and  $T_m$  stand for room temperature and melting temperature respectively, while m represents the thermal softening exponent. Notably, the impact of temperature and strain rate on the flow stress remains separate and uncoupled in this model. This implies that the sensitivity of strain rate isn't affected by changes in temperature, a characteristic not commonly observed in most metals.

Despite this simplification, the advantage of these models lies in their relative ease of calibration. They require minimal experimental data, typically involving a few stress-strain curves obtained at many different temperatures and rates [1].

#### 3.6.1 Modeling Parameters

The techniques employed to determine the modeling parameters described above can be briefly outlined [28]. The fundamental concept revolves around isolating each parameter by collecting data under specific conditions and employing appropriate graphical analysis. To achieve this, three sets of curves are constructed, illustrating the relationship between equivalent flow stress and equivalent plastic strain: one under quasi-static and isothermal conditions, and two corresponding to strains associated with the simulated phenomenon.

Parameter A represents the yield stress extracted from the quasi-static curve. Parameter B and exponent n necessitate a series of manipulations to be extracted.

The data associated with the elastic behavior ( $\varepsilon < \varepsilon_{yield}$ ) is disregarded, focusing solely on the plastic segment of the curve. Subsequently, the plastic data, represented as  $\sigma - \sigma_{yield}$

against plastic strain  $\varepsilon_{plastic}$ , is plotted on a log-log graph. Parameter B corresponds to the value of  $\sigma - \sigma_{yield}$  when  $\varepsilon_{plastic} = 1$ , while the exponent n is determined by the slope of the curve plotted on the log-log graph. Thermal softening exponent can be calculated using

$$m = \frac{\log(1 - \sigma/\sigma_{room})}{\log T^*} \text{ where } T^* = \frac{T - T_r}{T_m - T_r} \rightarrow (3)$$

Here,  $\sigma_{room}$  represents the stress corresponding to a specific plastic strain and strain rate observed at room temperature. On the other hand,  $\sigma$  stands for the stress associated with the identical plastic strain but under elevated temperature conditions.

### 3.7 Johnson Holmquist Strength Model

Contemporary ceramic armors showcase remarkable resistance against ballistic penetration, making ceramic armoring a prominent choice due to its inherent capability for "Interface defeat." Recent times have witnessed the emergence of various computational ceramic models. These encompass the Wilkin's ceramic model, which focuses on tensile failure, and the Rajendran-Grove model, grounded in micro-mechanics principles. Although consensus exists on ceramics' post-failure high compressive and pressure-dependent strength, the specific magnitude of this strength remains uncertain.

Addressing this issue, Johnson & Holmquist devised a pressure-dependent damage, strength, and fracture model. Within this framework, multiple iterations have been put forth, including JH-1, JH-2, and JHB. The core concept revolves around incorporating intact strength, failed strength, a damage model governing the shift from intact to failed strength, and a pressure model accounting for bulking effects. This transition hinges on inelastic strain, itself influenced by pressure. In the JH-1 model, intact material does not undergo softening during the damage process; instead, it experiences an abrupt drop to failed strength upon ( $D = 1$ ) complete damage. In contrast, the JH-2 model induces a progressive material softening as damage accumulates ( $0 < D < 1$ ). The JHB model treats damage and failed material in a manner akin to JH-1. However, it diverges by utilizing an analytical form for intact and failed material strengths while accommodating phase changes.

Both models JH-1 and JH-2 are incorporated into AutoDyn. JH-1 has demonstrated accurate simulation across a spectrum of test data and avoids gradual softening, which could introduce numerical inaccuracies.

### 3.7.1 Strength Model

As depicted by the graph provided, the strength profile is conceived to exhibit a linear rise, commencing at  $\sigma = 0$  for a tensile strength of  $-T$ , and progressing to a strength level of  $\sigma = S_1$  at a pressure of  $P_1$ . Here,  $T$  signifies the utmost hydrostatic tension that the material can endure. In conditions of tensile pressure, the material maintains elastic behavior until reaching a point of brittle failure. Subsequent to fracturing, the material forfeits its capacity to withstand any further tensile loading. Nevertheless, the impaired material continues to exhibit notable compressive strength, as evident from the  $D = 1$  curve.

The constants employed within the JH-1 model have been derived from Hopkinson bar tests, facilitating a comprehensive understanding of the material's response.

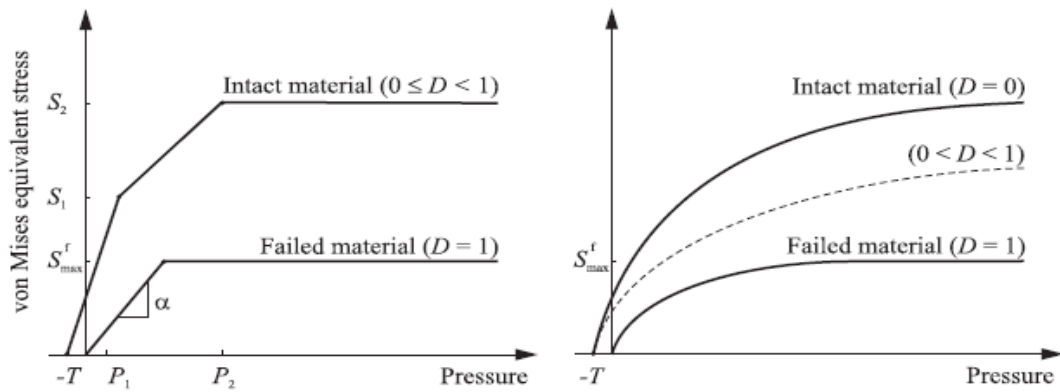


Figure 3-1: Von-Mises Equivalent Stress versus Pressure in JH-1(Left) and JH-2 (Right)

### 3.7.2 Damage Model

The gradual progression of softening as plastic strain increases is characterized by the accumulation of damage, and this phenomenon is modeled through the equivalent plastic strain denoted as  $\Delta\varepsilon^{-p}$ . Additionally, the equivalent plastic strain at which failure occurs, represented as  $\varepsilon_f^{-p}$ , is taken into account under a constant pressure scenario.

$$d = \frac{\sum \Delta\varepsilon^{-p}}{\varepsilon_f^{-p}} \rightarrow (4)$$

Where  $\varepsilon_f^{-p}$  is given by:

$$\varepsilon^{-p} = D_1(P^* + T^*)^{D_2} \rightarrow (5)$$

Using the constant parameters  $D_1$  and  $D_2$ , alongside the pressure values  $P^*$  and the minimum tensile hydrostatic pressure  $T^*$  required for failure, all of which are standardized in relation to the Hugoniot elastic limit  $\sigma_{HEL}$ .

### 3.8 Shock Wave Formation and Equation of State

In contrast to fluids where fluid particles move with the disturbance, waves in solids manifest as perturbations within the velocity field, traversing the continuum with diverse forms and velocities. The emergence of shock waves in the context of ballistic impact becomes an inevitable occurrence. Such scenarios fulfill all the prerequisites for the formation of shock waves, which encompass brief rise times, elevated levels of pressure and density, as well as fluctuating temperature amplitudes. Shock waves arise through a combination of wave superposition and dispersion effects. In instances involving nonlinear pressure-density relationships, these corresponding dispersion effects trigger the development of shock waves whenever swifter wave components surpass preceding waves with lower propagation speeds [29]. Hence, the nonlinear compressive behavior depicted below takes on the responsibility of inciting shock wave formation within solids.

$$c^2 = \left. \frac{\partial p}{\partial \rho} \right|_s = \left. \frac{\partial p}{\partial \rho} \right|_e + \frac{p}{\rho^2} \left. \frac{\partial p}{\partial \rho} \right|_\rho \quad \rightarrow (6)$$

The response of a material subjected to arbitrary three-dimensional stress conditions is typically represented by breaking down the stress tensor into two main components: the hydrostatic portion (pressure term) and the deviatoric components (plasticity term).

$$\sigma_{ij} = S_{ij} + \frac{1}{3}(\sigma_{11} + \sigma_{22} + \sigma_{33})\delta_{ij} = S_{ij} - p\delta_{ij} \quad \rightarrow (7)$$

In this context, the spherical tensor  $-p\delta_{ij}$  signifies the hydrostatic pressure component. When dealing with hydrodynamic material models like the Johnson-Cook model in the context of solid elements, an equation of state (EOS) becomes necessary due to the focus of hydrodynamic models on computing deviatoric stresses exclusively. The Equation of State is a requirement for the damage model Johnson-Cook when implementing the criterion of tensile failure involving pressure cut-off or dynamic spall.

To account for elevated pressures, efforts have been made to integrate pressure dependence into the yield criterion. It's generally assumed that the hydrostatic behavior remains independent of strain rate. The mathematical expression governing the interaction among the hydrostatic stress and strain components is termed the material's equation of state. Given that high-rate deformation leads to significant temperature generation under shock wave conditions, the formulation must also consider temperature or energy aspects.

The EOS serves as the three-dimensional constitutive equation that articulates the attainable states of the material under various conditions.

### 3.8.1 Rankine Hugoniot Relations

It is imperative to quantify the alteration in state variables subsequent to the passage of a shock. To achieve this, integral forms of conservation equations are employed to equate the conditions on both sides of the shock. This is carried out under the premise that the profile of the shock wave remains steady over time. The resultant relationships, acquired through the application of the principles of energy, mass and momentum conservation, are commonly referred to as the Rankine-Hugoniot equations.

$$\rho_o v_s = \rho_1 (v_1 - v_s) \quad \rightarrow (8)$$

$$p_1 - p_o = \rho_o v_s v_1 \quad \rightarrow (9)$$

$$p_1 v_1 = (\varepsilon_1 - \varepsilon_o) \rho_o v_s + \frac{1}{2} \rho_o v_s v_1^2 \quad \rightarrow (10)$$

These equations establish a connection between the density, internal energy and pressure behind the shockwave and their respective quantities ahead of the shockwave. This linkage is formulated in terms of particle velocity and shock velocity resulting from the shockwave. The Hugoniot curve, analogous to a stress-strain curve in uniaxial stress, represents a material property delineating the feasible shock states. It's important to note that while often referred to as the EOS, the Hugoniot curve is not a comprehensive formulation encompassing all states. Instead, it serves as a foundational component in the development of the EOS.

The EOS not only describes the attainable states a material can assume but also accommodates phase changes in situations where the shock energy is adequate to induce material melting.

### 3.8.2 Gruneisen EOS

In our specific scenario, the magnitude of shock energy will not reach the threshold required to induce a phase change. As a result, the Mie-Grüneisen EOS has been chosen to characterize the phenomenon of shockwaves within metallic sheets. The Mie-Grüneisen EOS can be conceptualized as an isochoric extrapolation derived from the shock Hugoniot. It's formulated as a Taylor series expansion centered around the Hugoniot pressure, allowing for a comprehensive representation of the material's behavior under shock conditions.

$$p(V, e) = p_H - \frac{\Gamma}{\Gamma} (e - e_H) \quad \rightarrow (11)$$

Here,  $\Gamma$  represents the Gruneisen constant, while  $p_H$  and  $e_H$  signify the state variables corresponding to the Hugoniot state.

### 3.8.3 Polynomial EOS

Traditionally, the understanding prevailed that ceramic fractures occurred due to tensile waves during ballistic impacts. However, recent findings have overturned this notion, revealing that ceramic fracture is primarily a consequence of high-pressure-induced plastic deformation. This deformation mechanism absorbs energy, diverging from the energy release associated with brittle fractures [31]. To simplify, the Hugoniot Elastic Limit can be perceived as the threshold for either fracture initiation or the initiation of plastic deformation. In the context of ceramics, transitioning from a Hugoniot incorporating longitudinal stress to an equation of state incorporating pressure isn't necessarily straightforward, as it necessitates a model accounting for material strength.

The disintegration of ceramic materials can be interpreted either as akin to a phase transformation or as a process involving damage accumulation. Both interpretations demand a mechanical model capable of capturing the alterations in material behavior following the initial shock. Hugoniot Elastic Limit (HEL) values for ceramics have been observed to be notably higher in comparison to metals. For instance, the HEL value for SiC is approximately 8 GPa. In the modeling of shockwave phenomena in ceramics, a polynomial EOS is often employed, with the exclusion of bulking effects. The pressure in this context is expressed as follows:

$$p(\zeta) = k_1\zeta + k_2\zeta^2 + k_3\zeta^3 + \Delta p \rightarrow (12)$$

Where  $k_1, k_2$  and  $k_3$  represent material constants, and  $\zeta = \rho/\rho_0 - 1$ , where  $\rho_0$  is the initial density. This quantity  $\zeta$  characterizes the compression. Additionally,  $\Delta p$  signifies the pressure increment stemming from dilatation, and its calculation is rooted in an energy conservation rationale. Initially,  $\Delta p$  remains at zero until the damage parameter  $D = 1$ , at which point  $\Delta p$  becomes a constant value and remains so.

### 3.9 Failure Model

The term "damage" in materials science is commonly associated with the initiation of cracks due to the growth of microvoids and microcracks, leading to a reduction in material strength. This process is often quantified using a dimensionless damage variable denoted as "D." This is defined by comparing the density of microvoids and microcracks  $\delta S_D$  on a plane intersecting the reference volume element's cross-section  $\delta S$ :

$$D = \frac{\delta S_D}{\delta S} \rightarrow (13)$$

Research carried out by Hancock and Mackenzie indicated that void coalescence lacks a preferred direction and isn't strictly constant across materials. They deduced that the critical equivalent fracture strain  $\varepsilon^f$  varies with stress triaxiality  $\sigma$ . They modeled  $\varepsilon^f$  to decrease with increasing hydrostatic tension  $\sigma_H$ . Johnson-Cook expanded upon the Hancock and Mackenzie model by introducing two additional parameters. From a numerical perspective, Johnson-Cook's model represents instantaneous failure, effectively reducing the stiffness of an element to zero after erosion. The damage to an element, denoted as "D," is:

$$D = \sum \frac{\Delta\varepsilon}{\varepsilon_f} \rightarrow (14)$$

In this context,  $\Delta\varepsilon$  denotes the increase in equivalent plastic strain that takes place during a single integration cycle. Material fracture becomes evident through element erosion as D reaches a value of one. Johnson-Cook's methodology employs a linear summation principle to account for modifications throughout the loading history. This approach acknowledges adjustments in the failure strain caused by factors such as temperature, strain rate, stress state, and along with the combination of specific types of damage during the loading sequence [1]. The overall equation for the strain at fracture is provided as follows:

$$\varepsilon_f = [D_1 + D_2 \exp D_3 \sigma][1 + D_4 \ln \tilde{\varepsilon}][1 + D_5 T^*] \rightarrow (15)$$

Here, the dimensionless strain rate is denoted as  $\tilde{\varepsilon} = \varepsilon/\varepsilon_o$ , with  $\varepsilon_o$  being the unit strain rate, and  $\tilde{\sigma} = \sigma_H/\sigma_{eq}$ , where  $\sigma_{eq}$  represents the von Mises equivalent stress given by  $\sigma_{eq} = \sqrt{\frac{2}{3} \sigma_{ij}^D \sigma_{ij}^D}$ . The parameters  $D_1 - D_5$  are part of the fracture model. The techniques employed to determine these parameters are briefly outlined step by step.

### 3.9.1 Triaxial Stress State ( $D_1, D_2,$ & $D_3$ )

To establish the exponential relationship between strain to fracture and stress triaxiality  $\sigma$ , a minimum of three axi-symmetric tensile tests is necessary. These tests are conducted under conditions of isothermality and quasi-static behavior. Various specimen shapes are utilized, each possessing an identical minimum cross-sectional diameter. The first specimen remains unnotched, while the second and third specimens incorporate specifically defined notch radii. The triaxial stress data collected from each of these specimens is then subjected to manipulation via curve-fitting techniques. This manipulation facilitates the plotting of strain to failure against the triaxial stress ratio. Subsequently, a least squares regression approach is employed to determine the parameters that yield the most optimal curve fit. This iterative process helps identify the parameters that align the best with the observed experimental data.



### 3.9.2 High Strain Rate Stress State ( $D_4$ )

To ascertain the mentioned parameter, torsion tests are performed across a spectrum of shear strain rates. These tests need to cover the entire high strain rate range pertinent to the simulated phenomenon. With the data on equivalent strain rate at fracture obtained from the quasi-static tests, a plot is created. This plot visually represents the correlation between strain at fracture and strain rate, encompassing a range from quasi-static rates to high strain rates. Furthermore, a curve is constructed on a naturally semi-logarithmic graph. This curve portrays a "reduced" strain to failure represented as  $\varepsilon_f - (D_1 + D_2)/(D_1 - D_2)$ . The slope of this curve is then determined, serving as a crucial parameter in the analysis.

### 3.9.3 High Temperature Environment ( $D_5$ )

The same methodology can be applied to compute  $D_5$  under high strain rate conditions. In this case, shear strain to failure is plotted against shear strain rate at various temperatures.  $D_5$  can then be calculated by plotting the "reduced" strain to failure, given by  $[\{\varepsilon_f - (D_1 + D_2)(1 + D_4 \ln \tilde{\varepsilon})\} / (D_1 + D_2)(1 + D_4 \ln \tilde{\varepsilon})]$ , against temperature.

The Johnson-Cook model has been incorporated into Autodyn to manage significant strains. It utilizes a backward-Euler integration algorithm that is fully vectorized for conducting analyses in three-dimensional (3D), shell, and two-dimensional (2D) scenarios. The simulation of crack propagation is achieved through an element removal process, where elements are eliminated when their damage surpasses a specified critical threshold,  $D_c$ .

Additionally, Johnson [33] proposed a non-dimensional parameter  $\rho V^2 / Y_d$  to classify the impact between two metallic bodies. Physically,  $\rho V^2$  represents the stagnation pressure of the projectile viewed as a fluid jet, and  $Y_d$  stands for the target strength. As the  $\rho V^2 / Y_d$  ratio surpasses 1, the inertia of the impacting projectile prevails over the strength of the target material.

## **CHAPTER 4: ANALYTICAL MODELING**

Analytical techniques serve as a valuable tool for addressing ballistic impact problems, effectively covering a substantial portion of the solution space. These models are rooted in algebraic relations and ordinary differential equations, minimizing the demand for extensive computational resources [20]. Ranging from simple 1D equations that encapsulate a singular physical phenomenon to more intricate 2D- or 3D models founded on local and global interactions, these techniques account for deformations and incorporate diverse failure criteria. Each model is crafted with the overarching objective of predicting the Ballistic Limit Velocity and Residual Projectile velocity for a specific protective shield.

Analytical models typically stem from qualitative laws, which can serve as a foundation for the development of new theoretical models and for guiding further experimental work [20]. However, the reliability of these models might vary based on the approach employed in their derivation. A model that yields accurate predictions in one scenario might not necessarily yield the same outcome in a different context. Ben-Dor and colleagues published a comprehensive review encompassing various models. This review covers a wide spectrum of approaches focused on elucidating the mechanics of high-speed ballistic penetrations.

### **4.1 Localized Interaction Approach**

In this framework, the combined outcome of interactions between a moving projectile and the host medium is envisioned as the accumulation of individual local exchanges between the surface elements of the projectile and the medium [23]. Each of these specific local interactions is influenced by the inherent geometric and kinematic characteristics of the surface element (predominantly dictated by the angle between the velocity vector and the local normal vector of the projectile surface) as well as certain overarching parameters that encapsulate integral properties of the medium, including hardness and density.

The localized interaction approach holds substantial appeal when addressing impact dynamics, as it provides a relatively straightforward means of characterizing projectile-medium interactions while considering the projectile's shape. This approach facilitates the simulation of projectile motion within a protective shield. It's worth noting that this approach is the most widely employed analytical modeling technique, and much of the work published by Ben-Dor is grounded in the principles of localized interaction modeling.

## 4.2 Cavity Expansion Approximation

The CEA approach is another frequently utilized analytical method. It revolves around the investigation of the growth of a symmetrical spherically cavity, initially of 0 radius, at a constant velocity. This expansion is scrutinized through a continuum mechanics model that characterizes the material's response. The pioneering work by Bishop and colleagues introduced the incorporation of cavity expansion models in the field of penetration mechanics. They formulated solutions that depict the quasi-static expansion of cylindrical and spherical voids within an infinite medium, commencing from an initial radius of zero. These solutions were subsequently employed to determine the forces acting on a conical projectile [23]. Within the context of cavity expansion approximation models, the solution is usually represented as:

$$p = \tilde{w}(\vec{a}; y) \rightarrow (16)$$

Here,  $p$  represents the stress at the boundary of the cavity, and  $y$  is the radius of the cavity.

The normal stress at the surface of a projectile moving in the same direction is given by:

$$\sigma_n = \tilde{w}(\vec{a}; uv) \rightarrow (17)$$

This implies that the normal stress due to the target-projectile interaction on the projectile's surface, located at a position with the instantaneous normal velocity  $v_n = v \cos \hat{\nu} = uv$ , is equivalent to the stress at the boundary of the cavity expanding with a constant velocity  $v_n$ .

The two most commonly used variants of this technique are the Spherical Cavity Expansion Approximation (SCEA) and the Cylindrical Cavity Expansion Approximation (CCEA).

In the case of CCEA, when studying the normal penetration of a slender body, the target material is assumed to move radially. The target is divided into infinitesimally thin layers, and the expansion of the cavity due to the impacting projectile is analyzed for each layer. This approach provides the stress at the boundary of the cavity in each layer, subsequently leading to the determination of the force exerted on the projectile at each location along its lateral surface.

## 4.3 Lambert-Jonas Approximation

After a thorough examination of various empirical and semi-empirical models, Lambert and Jonas introduced a unified relationship for evaluating ballistic impact phenomena. They proposed a power-law relation connecting residual velocity, ballistic limit velocity and impact velocity. Many of the empirical and semi-empirical models can be expressed in the form of Eq-1, mainly those grounded in principles of energy and momentum conservation. Researchers like Mileiko, Sarkisyan, and Mileiko et al. demonstrated that solving the

projectile's equation of motion results in Eq-1 with  $a_0 = 1$  when the projectile's drag force and velocity exhibit a power-law relationship. Nixdorff demonstrated that under specific assumptions, the theory proposed by Awerbuch and Awerbuch and Bodner leads to Eq-1. Ben-Dor et al. evaluated the precision of Eq-1 or a general exponent  $n$  in comparison to its accuracy when  $n = 2$ . Garbarek and Andreson et al., however, viewed Eq-1 as just one possible correlation between  $\hat{v}_{res}$  and  $\hat{v}_{imp}^n$ , and introduced an alternative unified relationship.

The equation for residual velocity  $\hat{v}_{res}$  as a function of impact velocity  $\hat{v}_{imp}^n$  with approximation coefficients  $a_i (i = 0,1,2)$  is given by:

$$\hat{v}_{res} = (a_2 z^2 + a_1 z + a_0 z^{0.5}) / (z + 1), z = \hat{v}_{imp} - 1, z \leq 2.5 \rightarrow (18)$$

Here, the coefficients  $a_i$  are determined through regression analysis of experimental data. In contemplating the development of more complex models for ballistic penetration, Bodner raises the question of whether such efforts are worthwhile, given that they may seem to bring the approach closer to full numerical solutions.

#### **4.4 Commonly Used Analytical Models and Their Application**

Numerous analytical models have been developed to measure the ballistic performance of different materials. Models such as those presented by Wen and Jone, Bodner, and Bai and Johnson have contributed to this domain. Recht and Ipson introduced a discrete version of the localized interaction theory, employing the ballistic pendulum technique and assuming shear plug formation as the sole failure mechanism. However, their model had limitations due to its requirement for prior knowledge of the Ballistic Limit Velocity (BLV) and a single failure mechanism.

Among these, dynamic cavity expansion models stand as particularly effective analytical tools for studying the dynamics of rigid projectiles. A significant advancement in this direction came from Chen and Li [32], who introduced a penetration model for thick plates featuring projectiles with different shapes. Their model encompassed two perforation mechanisms: hole expansion and plug formation for sharp- and blunt-nosed projectiles, respectively. Going beyond localized shear deformation at the boundary of the central plug, their rigid plastic structural model incorporated plate bending and membrane stretching effects. The local indentation/penetration employed a dynamic cavity model [32]. They later enhanced their model to encompass failure modes ranging from shear plugging to adiabatic

shear plugging as the target thickness increases. They formulated the Ballistic Limit Velocity  $V_{BL}$  and residual projectile velocity  $V_r$  as follows:

$$V_{BL} = 2\sqrt{\frac{2x(1+\eta)(\eta+\vartheta)}{\sqrt{3}}}. \sqrt{\frac{\sigma_y}{\rho}} \rightarrow (19)$$

$$V_r = \frac{\vartheta V_i + \sqrt{(V_i^2 - V_{BL}^2)}}{(1 + \eta)(\eta + \vartheta)} \rightarrow (20)$$

Where  $x = H/d$  with  $H$  as the thickness of the circular target plate and  $d$  the diameter of the impacting projectile. Also,  $\eta = \rho\pi d^2 H/4M$  with  $M$  as the mass of the projectile, while  $\sigma_y$  and  $\rho$  are the yield stress and density of the target material.

In the realm of composite armor, a common configuration includes a ceramic front plate and a ductile back plate, often made of aluminum. Florence developed an analytical model to accurately predict the ballistic performance of such targets impacted perpendicularly by a rigid projectile. This model was later refined by Hetherington and Rajagopalan. For this kind of armor, Florence's model is expressed as:

$$v_{bl}^2 = \frac{\varepsilon_2 \sigma_2 b_2 Z[(\gamma_1 b_1 + \gamma_2 b_2)z + m]}{0.91m^2}, z = \pi(R + 2b_1)^2 \rightarrow (21)$$

Where  $b_i$  represent the thickness of plate,  $\sigma_i$  is the ultimate tensile strength,  $\varepsilon_2$  is braking strain,  $\gamma_i$  denotes the densities of the target materials. The subscripts 1 and 2 pertain to the ceramic and back plates, respectively. Florence's model is especially well-suited for addressing issues concerning armor optimization.

Ben-Dor and colleagues [2006a] carried out analytical investigations regarding the impact of air gaps between plates and the arrangement of plates on the Ballistic Limit Velocity (BLV) of a multilayered shield against conical impactors. They observed that, across a wide spectrum of models describing the interaction between the impactor and the shield, the shield's ballistic performance remains unaffected by variations in air gap widths and the order of plates, provided the plates are composed of the same material. Utilizing the two-term impactor-shield interaction model, they formulated a criterion based on mechanical properties that establishes the optimal sequence of plates for achieving the highest BLV. Importantly, this criterion retains its validity even for projectiles with shapes other than conical.

## CHAPTER 5: NUMERICAL SETUP

### 5.1 Simulation Parameters

In this chapter, we outline the essential parameters and inputs required for Finite Element Method (FEM) simulations of projectile impacts on both monolithic and multi-layered sheets. For monolithic sheets, circular plates with a diameter of 500 mm and thickness ranging from 10 to 20 mm were chosen as target specimens. Multi-layered sheets consisted of two or three bonded sheets with similar or varying thicknesses. The chosen projectile was a blunt cylinder measuring 20 mm in diameter and 80 mm in length. Initially, the projectile material was set to Arne Tool Steel, as employed by Borvik in their experimental study on the ballistic impact of blunt projectiles against Weldox 460E steel plates of various thicknesses.

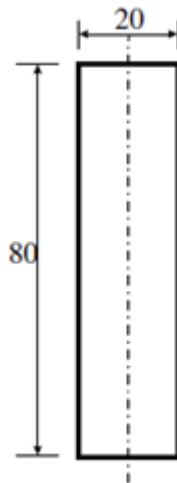


**Figure 5-1: Dimensions of Blunt Faced Projectiles**

All simulations were conducted with the projectile's velocity ranging from 200 to 500 m/s, primarily to identify a singular performance parameter applicable to different armor configurations. Initially, both the projectile and target were modeled as 2D axisymmetric geometries to ascertain if the chosen approach could address various penetration scenarios. The decision to model the projectile as a rigid body was based on the experimental findings showing minimal deformation of the projectile. This choice was made to optimize computational efficiency. The critical impact area was assumed to be 1.5 times the projectile's diameter. This assumption was employed to create a coarser mesh towards the outer boundary of the plate. An important aspect to consider before proceeding with the final simulation is the issue of hourglass energy. While the one-point (reduced) integration technique used in ANSYS Explicit Analysis offers robust solutions for large deformations

and high strain rates, it is susceptible to zero-energy modes. These modes, often referred to as hourglassing modes, exhibit oscillatory behavior with significantly shorter periods than the overall structural response. They lack stiffness and cause a zigzag appearance in the mesh, leading to what is known as hourglass deformations. The hourglass mode does not induce strain and consequently does not contribute to the energy integral. Although this issue cannot be entirely eliminated, especially when utilizing brick and quadrilateral shell or 2D elements, ANSYS suggests a straightforward solution to mitigate hourglassing. This involves using a uniform and refined mesh during numerical simulations. ANSYS proposes a simple criterion that the hourglassing energy should always remain below 10% of the internal energy. In the critical impact area, the element size was set at 0.125 mm, which was chosen as a fine mesh option to strike a balance between computational accuracy and time efficiency.

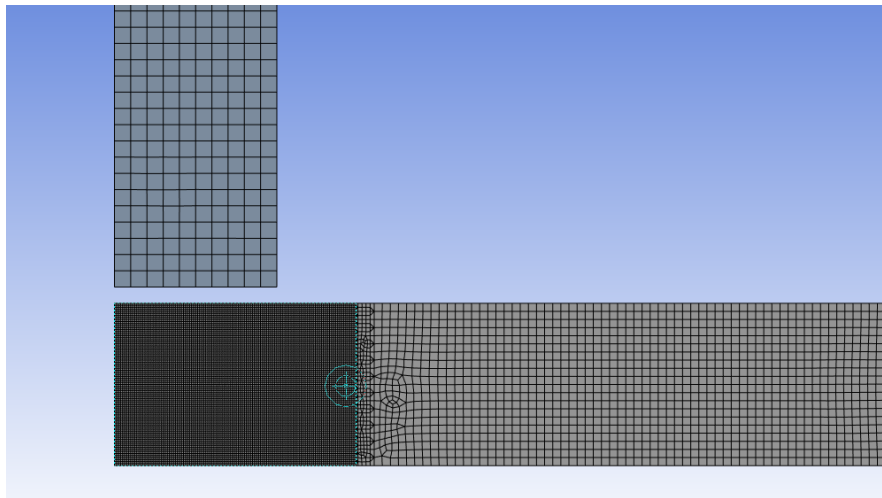


**Figure 5-2: Mesh of Blunt Projectile and Target**

AutoDyn offered two options for simulation: one was to employ an ideal scenario where all projectile-target interactions were modeled as frictionless, and the other was to include a friction coefficient. In the case of simulating the penetration of a blunt projectile into a target sheet, the effect of friction was disregarded. This decision was primarily based on the absence of a thin film between the two interacting surfaces [37]. This is because, upon impact, the front edge of the blunt projectile deforms, resulting in a mushroomed shape. As the front portion of the projectile penetrates the target, it creates a cavity typically larger than the diameter of the remaining projectile body. As a result, there is minimal contact between the remaining projectile body and the target.

## 5.2 Mesh Independence Study

Considering the projectile and target shapes, a structured mesh appeared to be a practical and effective choice. The total number of elements for a 10 mm 2D circular plate amounted to 13,989.

Borvik's observations indicated that numerical results were notably sensitive to mesh sizes in scenarios involving blunt projectiles, in contrast to conical nose projectiles [40]. Consequently, a study was conducted to establish mesh independence. This aimed to assess the impact of varying mesh sizes on numerical accuracy and computational solution reliability. To this end, a blunt projectile was tested against a 10 mm thick Weldox 460 E target at an impact velocity of 241.5 m/s. Experimentally, the residual velocity of the projectile was measured at 165.9 m/s [3]. A mesh independence study was performed by systematically increasing the mesh size up to 0.5 mm. The residual velocity was recorded for each case and compared against the experimental result. The following table outlines the variations in residual velocity and computational time for each mesh size.

A difference of 26.36% was noted for mesh sizes exceeding 0.25mm, a value significantly higher than the 5% threshold. Consequently, a mesh size of 0.125mm was ultimately chosen due to its optimal balance between accuracy and simulation time.

**Table 5-1: Mesh Independence Study**

Sr. No.	Minimum Element (mm)	Residual Velocity (m/s)	% Difference	CPU Time (Hr)
1	0.075	171.92	-	5.6
2	0.1	171.68	0.14	2.5
3	0.125	171.39	0.17	1.2
4	0.15	163.34	4.93	0.9
5	0.2	155.23	5.22	0.6
6	0.25	122.17	27.06	0.4



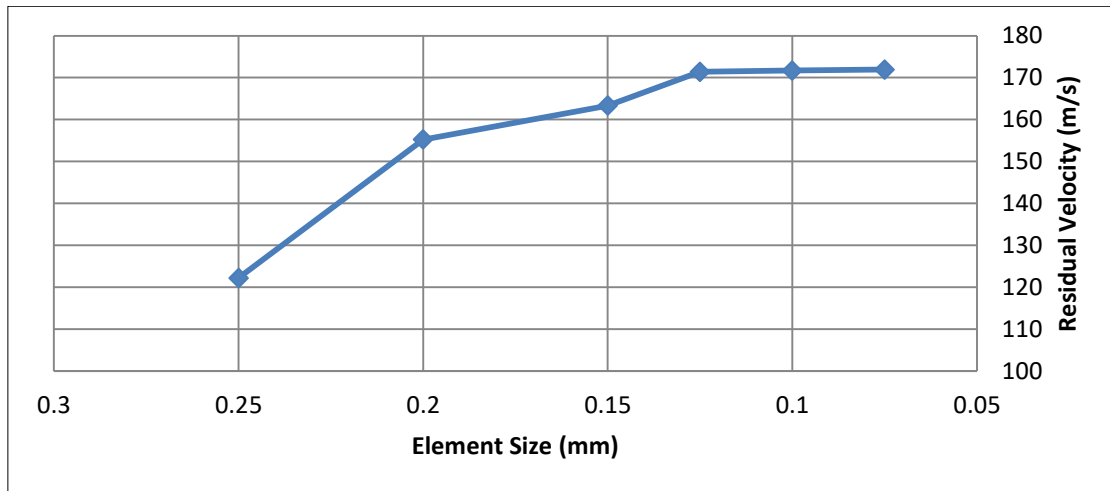


**Figure 5-3: Mesh Independence Study**

### 5.3 Material Properties

The shockwave phenomenon in ceramics was simulated using a Polynomial EOS with bulking deactivated, whereas a linear shock EOS model was implemented for metallic targets.

Ductile materials utilized the Johnson-Cook strength and damage model, while brittle target materials employed the JH-1 model. The default material parameters in the ANSYS library were suitable for capturing ballistic events concerning Silicon Carbide and Al 7075 T6. However, this was not the case for Weldox 460E, as no relevant data was available. To address this, an extensive review of relevant literature was conducted to identify the essential material parameters for modeling the Johnson-Cook strength and failure models. Subsequent to meticulous research, the following material parameters were selected.

**Table 5-1: Material Properties and Modeling Parameters for Metallic Shields**

Sr. No	Parameter	Weldox 460E	Unit
1	Density	7850	$kg/m^2$
2	Specific Heat	452	$J/kg.K$
3	Johnson Cook Strength		
3.1	Initial yield Stress $A$	490	$MPa$
3.2	Hardening Constant $B$	807	$MPa$
3.3	Hardening Exponent $n$	0.73	-
3.4	Strain Rate Constant $C$	0.0114	-

3.5	Thermal Softening Exponent $M$	0.94	-
3.6	Melting Temperature	1800	$K$
3.7	Shear Modulus $G$	75	$GPa$
4	Shock EOS Linear		
4.1	Gruneisen Coefficient	1.707	-
4.2	Parameter $C_0$	3850	$m/s$
4.3	Parameter $S$	1.354	-
5	Johnson-Cook Failure		
5.1	D1	0.0705	-
5.2	D2	1.732	-
5.3	D3	-0.054	-
5.4	D4	-0.015	-
5.5	D5	0	-

In scenarios where a projectile interacts with the target material, defining the nature of this interaction becomes paramount. Particularly in instances involving substantial deformations like ballistics, precise modeling of contact interfaces is imperative to ensure accurate numerical outcomes. When the trajectory-based contact detection was employed within ANSYS AutoDyn, two options were presented: the "Penalty contact constraint," which hinged on the contact segment's size and its material characteristics, and the "Decomposition response," which computed the system's response to detected contact in order to conserve energy and momentum. In comparison to the penalty method, the decomposition response algorithm exhibited greater impulsiveness, resulting in elevated hourglass energies and energy errors.

Throughout all simulations, it was assumed that the projectile impacted the target sheet at a perfectly perpendicular angle. A velocity probe was strategically placed at the rear end of the projectile to monitor its velocity during penetration, given that the front end could undergo substantial deformation in specific scenarios.

# CHAPTER 6: NUMERICAL RESULTS

Throughout this study, diverse target setups comprising parallel layers and solid plates will be explored. The initial phase involves conducting numerical simulations utilizing experimental data derived from sources such as Borvik [2, 3]. This undertaking serves a dual purpose: not only does it provide a benchmark for verifying our computational outcomes, but it also assumes a crucial role in identifying critical computational parameters and methodologies.

## 6.1 Blunt Projectiles against Monolithic Sheet

### 6.1.1 Weldox 460E

Initially, simulations were undertaken for Weldox 460E due to the substantial volume of available experimental and numerical data for comparative analysis. The study commenced by considering the scenario of a blunt Arne Tool Steel projectile impacting a circular plate with a thickness of 10 mm. The projectile was propelled at a velocity of 500 m/s.

Throughout the simulation process, an energy summary was meticulously recorded. Upon the projectile's impact with the target, a reduction in kinetic energy was observed, which correspondingly manifested as an internal energy increase of precisely 604.8 J. Consequently, the principle of energy conservation was duly satisfied. As previously discussed, explicit hydrocodes incorporate reduced point integration to counteract the occurrence of locking phenomena, thus mitigating the emergence of erroneous deformation modes.

The subsequent step entailed evaluating the hourglass energy, as AutoDyn employed hourglass control to manage zero-energy modes. The computed hourglass energy remained well within the threshold of 10% in relation to the internal energy, in accordance with ANSYS recommendations.

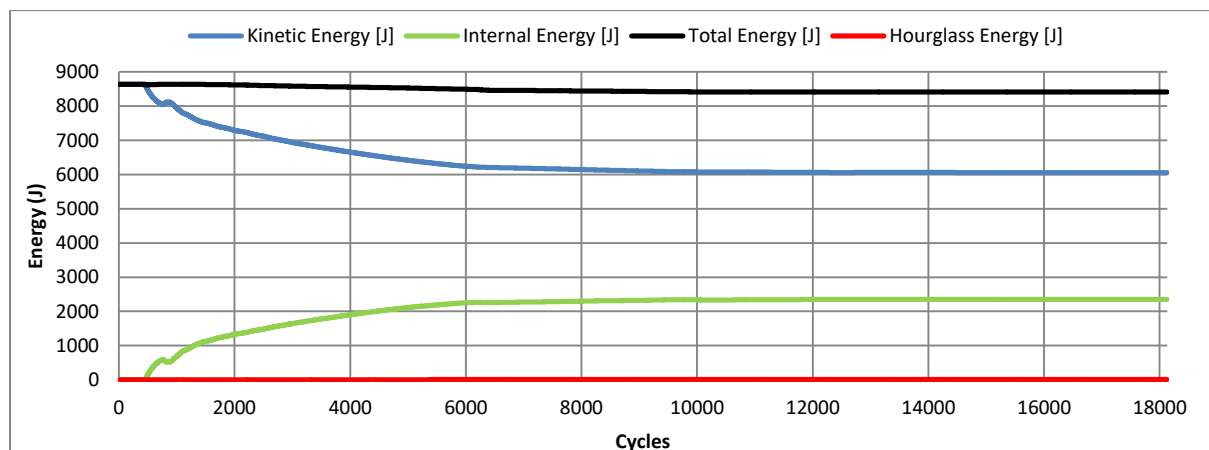
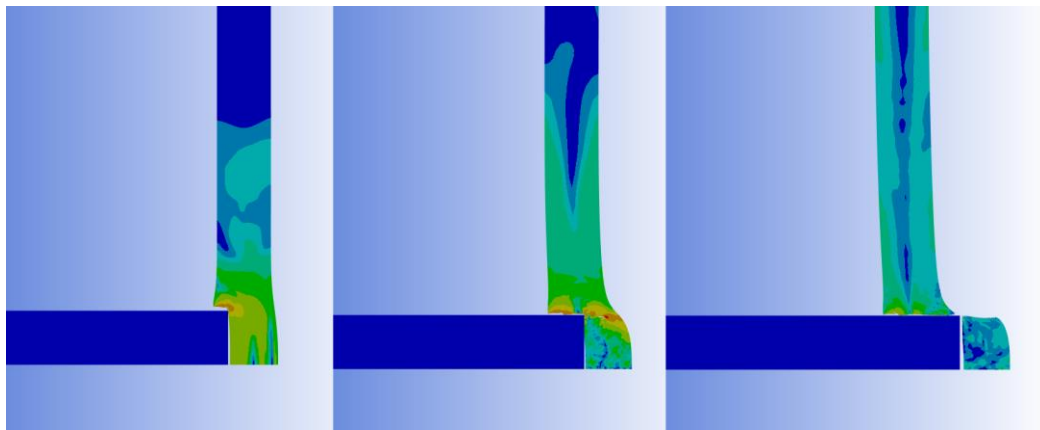


Figure 6-1: Energy Comparison

The predominant reason for the target's failure was attributed to plugging, a scenario commonly observed when dealing with blunt projectiles. The sharp edges of the projectile induced the formation of cracks in the surrounding circumference. This phenomenon aligns with the proposition put forth by Woodward, indicating that plugging is the prevailing failure mode when the thickness of the target plate is less than  $\sqrt{3d_p}/2 = 17.3mm$ , where  $d_p$  represents the projectile's diameter. It's essential to note that such failures rarely exhibit complete domination by a single mode.

As depicted in the figure, there is also a slight degree of ductile hole enlargement evident. Adhering to a failure mode driven by adiabatic shear, the deformation predominantly localizes around the projectile's sharp edges, as visually demonstrated in the subsequent figure.



**Figure 6-2: Penetration in Weldox 460E, Initial Velocity = 296m/s**

A noticeable gap becomes apparent between the projectile body and the perimeter of the cavity. This gap indicates minimal contact between the projectile's body and the target due to the projectile having penetrated through the target material.

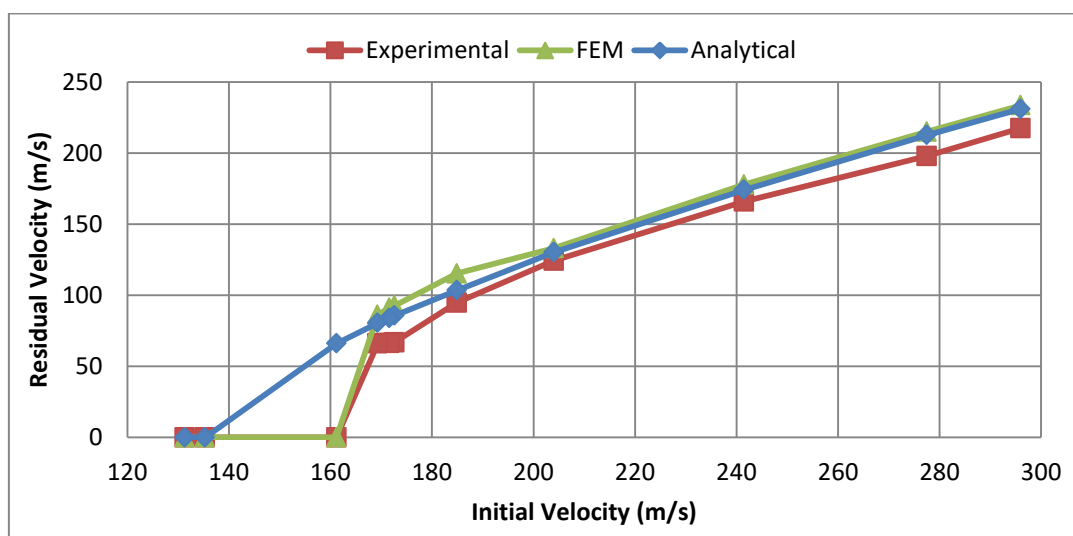


**Figure 6-3: Experimental [3], Analytical & Numerical Solution of Weldox 460E**

A graph has been generated for ten different input velocities, ranging from 131.3 m/s to 296 m/s. The graph was plotted without employing any curve fitting techniques. The ballistic limit velocity for the aforementioned target was determined to be 161 m/s. Notably, a sharp decline in residual velocity occurred below an impact velocity of 170 m/s.

The analytical solution was calculated utilizing the approach introduced by Chen and Li, which relies on the rigid plastic analysis of plug motion and the local penetration process [41]. The outcomes obtained from the analytical method fell within the range of the numerical and experimental findings. However, the analytical model exhibited imprecise outcomes at lower velocities, yielding a ballistic limit velocity of 135 m/s.

The experimental outcomes consistently fell below the numerical ones. As the initial velocity approached the ballistic limit velocity, a minor increase in the error between experimental and numerical results was observed. This trend is depicted in the provided graph, underscoring the substantial comparability between the numerical and experimental datasets.

### 6.1.2 Al 7075 T6

The simulation results have been derived for a scenario where a 10 mm Al 7075 T651 target is subjected to the impact of a blunt projectile composed of Arne tool steel, moving at a velocity of 400 m/s.

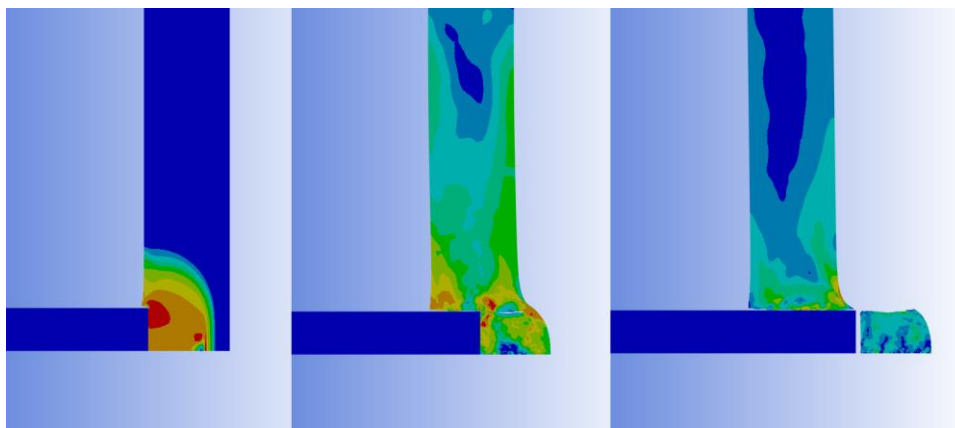


**Figure 6-4: Penetration in Al 7075 T6, Initial Velocity = 400m/s**

Al 7075 T6 exhibits a failure mode similar to that of steel. A plug, approximately the size of the projectile diameter, emerges at the rear of the target. Elevated shear stress regions are generated around the perimeter of the projectile, leading to the practical shearing of the plug out of the target. The subsequent graph has been plotted to depict the impact of a blunt projectile on a 20 mm AA 7075 T6 target. The initial velocities span from 150 m/s to 400 m/s. The graph illustrates that the numerical outcomes closely match the experimental results, indicating that the current numerical setup is suitable for conducting additional simulations.

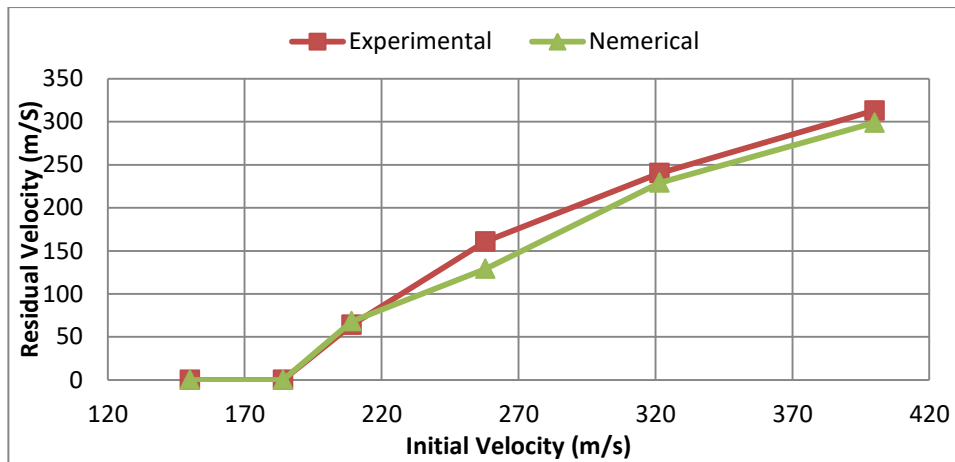


Figure 6-5: Comparison of Experimental & Numerical Solution Al 7075 T6

### 6.1.3 Silicon Carbide

When a material's tensile strength is lower than its compressive strength, the initial compressive stress wave leads to radial fractures. This particular mode of failure is evident in SiC, as depicted in the figure below. The initial velocity of the projectile set to was 500 m/s for that the residual velocity was determined to be 420 m/s.

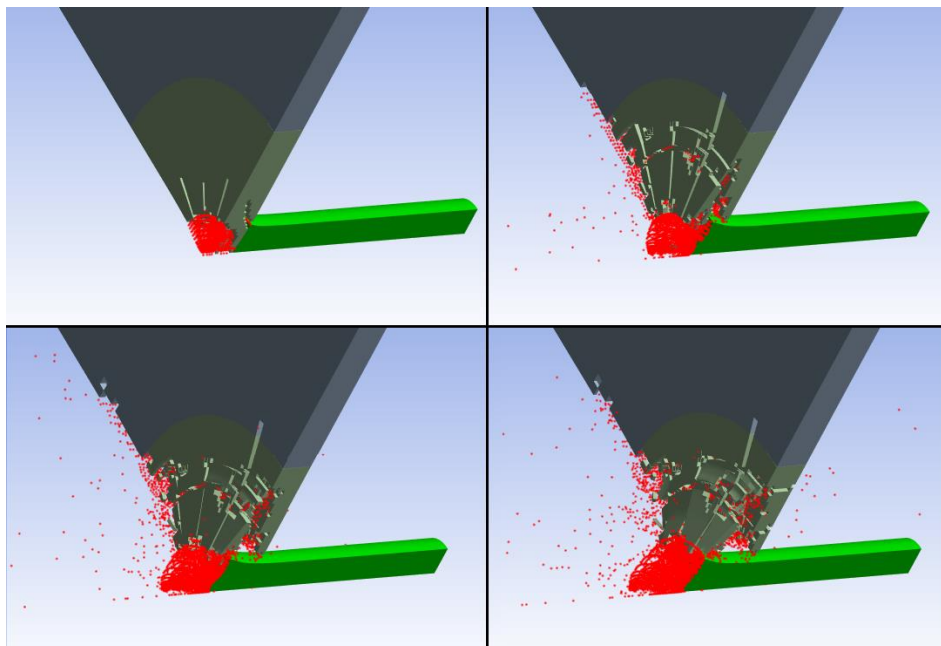
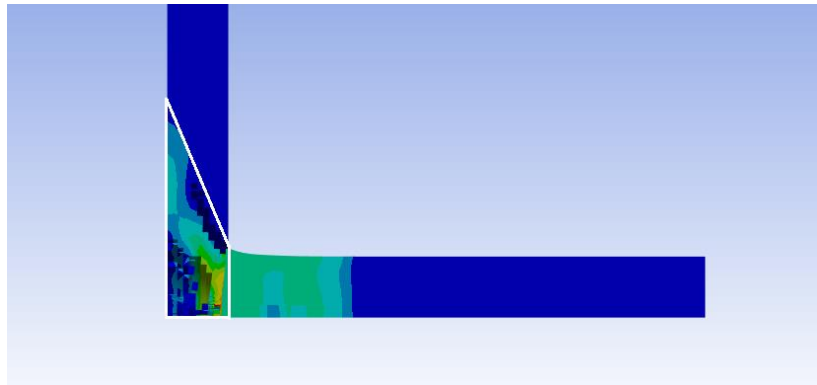


Figure 6-6: Crack Propagation in SiC

Signs of damage manifest on the rear surface of the target plate, taking the form of radial cracks. The material experiences instantaneous failure upon impact, without any signs of bulking. Unlike metals, there is no indication of plugging; rather, a substantial amount of pulverization is observed in front of the projectile. Silicon Carbide fails due to the high-pressure-induced pulverization effect. As illustrated, the damage on the front side of the

target is minimal compared to the rear side, highlighting the brittle nature of the material's failure. The initiation of damage commences at the periphery of the contact area between the projectile and the target.



**Figure 6-7: Stress Wave Propagation Conoid in SiC**

The highlighted conoid, shown in white, illustrates the propagation of the stress wave in both longitudinal and lateral directions. This phenomenon arises from the initial compressive stress wave, which, upon reflection from the target's free end, generates a longitudinal wave causing the plate to fracture along the indicated white line. The maximum tensile principal stress materializes just outside the periphery of the contact region, giving rise to a cone-shaped crack that propagates towards the rear of the ceramic.

The precise propagation angle of this wave is 68.5 degrees. This angle, denoted as "68.5," corresponds to the trajectory of the minimum principal stress. This choice is made due to the fact that by propagating along trajectories of minor principal stresses, cracks remain orthogonal to the primary tension component, thus maximizing the strain energy release rate. The propagation angle for this wave was determined by measuring the upper and lower cone diameters. While the condition was met, it was noted that crack propagation did not strictly follow a straight path; instead, it resembled a semi-elliptical trajectory. The minor-to-major axis ratio of this ellipsoid was approximately 0.32.

Another crucial phenomenon associated with ceramics, including SiC, is the interface defeat phenomenon, also known as projectile deformation upon impact. A simulation result effectively illustrates the type of strain that a blunt projectile undergoes. A flat-ended projectile striking a target with substantial compressive strength leads to noticeable projectile deformation, manifesting as mushrooming on the impact end.

Unlike metals, ceramics are not typically utilized as standalone options for monolithic targets. However, when combined with metallic sheets, ceramics play an enhanced role in providing significant ballistic resistance.

## 6.2 Multi-Layered Targets

### 6.2.1 Weldox 460E – SiC

Ceramics possess three pivotal attributes: low density, high compressive strength, and exceptional hardness. Often, ceramics like Alumina and SiC are amalgamated with malleable materials, primarily aluminum. Due to their robust compressive strength, ceramics deform projectiles significantly, simultaneously sapping a substantial portion of the projectiles' kinetic energy. This leads to the projectiles being eroded and decelerated, making them readily interceptable by the subsequent ductile rear plate. Consequently, the optimal choice is a bilayered sheet comprising SiC as the frontal layer and Weldox 460E as the rear plate.

The aim of this study was to determine the optimal combination of plate thicknesses for Weldox 460E and SiC that could match the performance of a 10mm monolithic Weldox 460E plate while minimizing weight. The results were obtained by testing various combinations of thicknesses for both materials. The range of thickness variations was from 1mm to 6mm for Weldox 460E and from 1mm to 10mm for SiC. The setup involved a SiC front plate and a Weldox 460E back plate, placed without any gap between them.

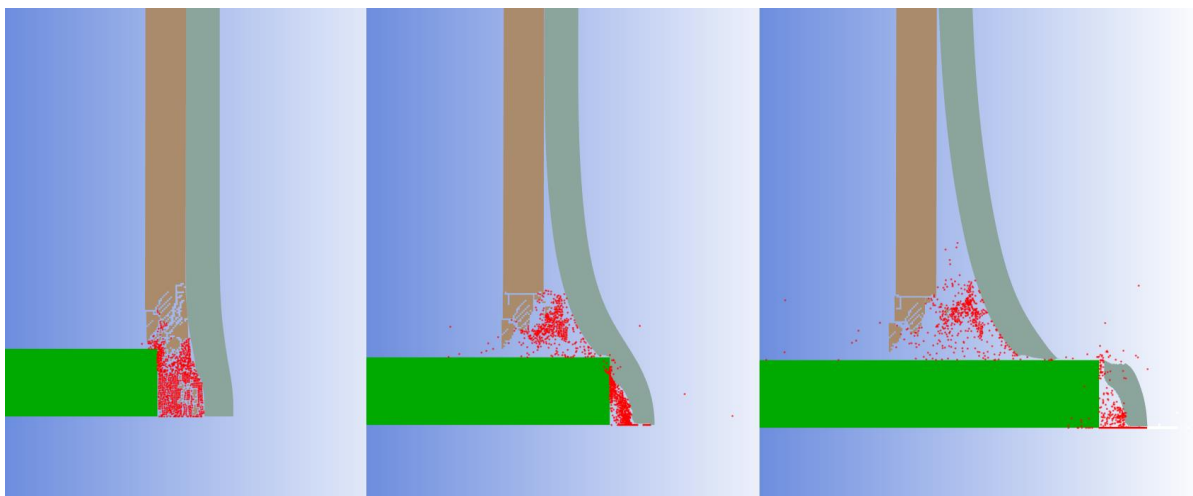


**Figure 6-8: Penetration in Weldox 460E - SiC, Initial Velocity = 296m/s**

The Initial velocity was set to 296 m/s. As shown in the figure above SiC fractures instantaneously on impact and the eroded elements move towards the back plate and push it back word, finally the back plate fails through plugging. The following table presents the residual velocities for different configurations:



**Table 6-1: Residual Velocity for Varying Thickness of Weldox 460E - SiC, Initial Velocity = 296m/s**

W460 E	SiC									
	1 mm	2 mm	3 mm	4 mm	5 mm	6 mm	7 mm	8 mm	9 mm	10 mm
1 mm					270.1	267.8	264.1	260.2	256.2	252.6
2 mm					260.1	256.2	251.9	249.0	243.8	238.6
3 mm					250.1	246.4	243.4	239.9	235.8	229.5
4 mm					242.8	239.0	235.7	231.6	228.5	221.0
5 mm					234.4	228.9	227.0	224.8	220.7	216.5
6 mm	254.8	240.0	231.7	226.6	223.1	219.0				

In the table above, the results that are highlighted in green indicate values lower than 233.49 m/s which was the residual velocity of 10mm Weldox 460E plate. This implies that these particular combinations perform as well as or even better than the 10mm Weldox 460E plate, given an initial velocity of 296 m/s. Additionally, results were also collected for an initial velocity of 161.2 m/s, at which point the 10mm Weldox Sheet was able to completely stop the projectile.

**Table 6-2: Residual Velocity for Varying Thickness of Weldox 460E – SiC, Initial Velocity = 161.2m/s**

W460 E	SiC									
	1 mm	2 mm	3 mm	4 mm	5 mm	6 mm	7 mm	8 mm	9 mm	10 mm
3 mm										75.9
4 mm							84.3	84.7	81.8	0
5 mm						48.2	0	0	0	0
6 mm	0	0	0	0	0	0				

In this table, the results highlighted in green indicate velocities less than 0 m/s. This implies that these specific combinations completely halt the projectile when subjected to an initial velocity of 161.2 m/s, yielding the same outcome as the 10mm Weldox 460E plate. Subsequently, the total weights of these combinations were computed for a standard rectangular armor plate measuring 300mm in height and 250mm in width. The density of Weldox 460E is 7850 kg/m<sup>3</sup>, while for SiC, the density is 3215 kg/m<sup>3</sup>. The subsequent table displays the weights in kilograms (kg) for various combinations. As a point of reference, the weight of the 10mm Weldox 460E plate is 5.89 kg.

**Table 6-3: Weight (kg) for Varying Thickness of Weldox 460E – SiC**

W460 E	SiC									
	1 mm	2 mm	3 mm	4 mm	5 mm	6 mm	7 mm	8 mm	9 mm	10 mm
3 mm										4.18
4 mm							4.04	4.28	4.53	4.77
5 mm					4.15	4.39	4.63	4.87	5.11	5.36
6 mm	3.77	4.01	4.26	4.50	4.74					

The purpose of this table was to identify the lightest combination of Weldox 460E and SiC that that can match the performance of a 10mm Weldox 460E plate. The result highlighted in blue—consisting of 6mm of Weldox 460E and 3mm of SiC—is the lightest configuration, weighing in at 4.26 kg, while delivering equivalent performance to the 10mm Weldox 460E plate. Subsequently, a ballistic curve was plotted for this particular combination, varying the projectile's initial velocity between 161.2 m/s and 296 m/s.

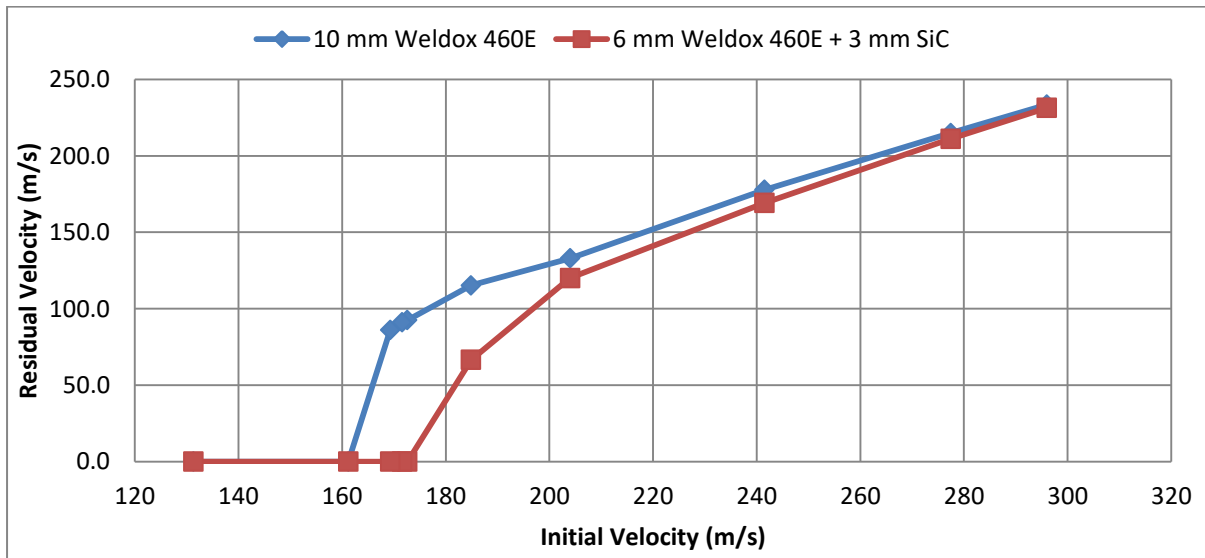


**Figure 6-9: Ballistic Curve for Combination of 6mm Weldox 460E and 3mm SiC**

This graph illustrates that the chosen multilayered target performs notably better at velocities below 200 m/s, resulting in considerably lower residual velocities compared to the 10mm monolithic target. However, as the velocity increases, the results converge, and at an initial velocity of 296 m/s, both targets yield nearly identical residual velocities.

This curve provides evidence that the combination of 6mm Weldox 460E and 3mm SiC outperforms or matches the performance of the 10mm Weldox 460E at all initial velocities. Moreover, this combination weighs 4.26 kg, making it 1.63 kg lighter than the 5.89 kg weight of the 10mm Weldox 460E plate. If an individual were to wear two plates of this armor, one in the front and one in the back, the total weight would be 8.52 kg. In contrast, the weight of the 10mm Weldox 460E plate of 11.78 kg. This reduction in weight by 3.26 kg is significant, particularly when considering that the armor would be worn for extended periods of time.

## 6.2.2 Al 7075 T6 – SiC

The identical study was conducted for the pairing of Al 7075 T6 and SiC. The outcomes were derived by altering the thickness within the range of 6mm to 13mm for Al 7075 T6 and 1mm to 10mm for SiC. In this setup, the SiC plate served as the front layer, while the Al 7075 T6 plate was positioned as the back layer, ensuring no spacing between them.

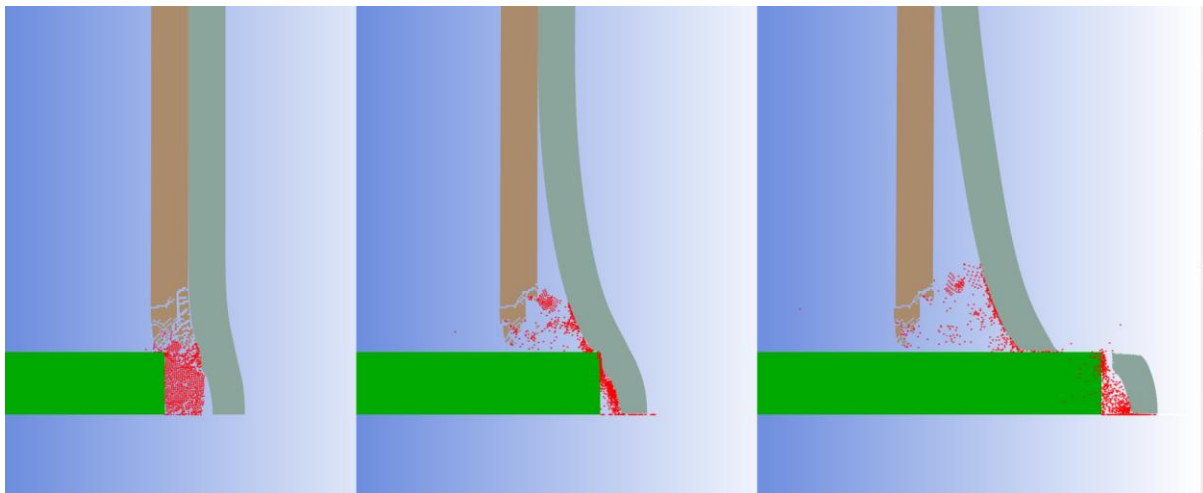


**Figure 6-10: Penetration in Al 7075 T6 - SiC, Initial Velocity = 296m/s**

The initial velocity was set to 296 m/s. As illustrated in the figure above, SiC fractures immediately upon impact, causing the eroded particles to propel towards the back plate, resulting in a backward displacement. Ultimately, the back plate fails due to plugging. The subsequent table provides the residual velocities for various configurations:

**Table 6-4: Residual Velocity for Varying Thickness of Al 7075 T6 – SiC, Initial Velocity = 296m/s**

Al 7075 T6	SiC									
	1 mm	2 mm	3 mm	4 mm	5 mm	6 mm	7 mm	8 mm	9 mm	10 mm
6 mm								238.6	237.2	233.9
7 mm								237.1	230.2	227.0
8 mm							236.6	233.7	226.2	225.8
9 mm						237.0	227.5	226.2	221.5	
10 mm				241.9	236.1	234.7	229.9			
11 mm			239.7	238.8	221.4	232.6				
12 mm		239.4	233.6	226.6						
13 mm	240.6	233.3	230.3							

The green-highlighted outcomes represent values below 233.49 m/s. Data was also gathered for an initial velocity of 161.2 m/s. For every combination highlighted in green within the previous table, the residual velocity measured 0 m/s when the initial velocity was set to 161.2 m/s. The following table illustrates the weights in kilograms (kg) for different combinations. Al 7075 T6 has a density of 2804 kg/m<sup>3</sup>, while SiC has a density of 3215kg/m<sup>3</sup>.

**Table 6-5: Weight (kg) for Varying Thickness of Al 7075 T6 – SiC**

Al 7075 T6	SiC									
	1 mm	2 mm	3 mm	4 mm	5 mm	6 mm	7 mm	8 mm	9 mm	10 mm
6 mm								3.19	3.43	3.67
7 mm								3.40	3.64	3.88
8 mm							3.37	3.61	3.85	4.09
9 mm						3.34	3.58	3.82	4.06	
10 mm				3.07	3.31	3.55	3.79			
11 mm		2.80	3.04	3.28	3.52	3.76				
12 mm	2.76	3.01	3.25	3.49						
13 mm	2.98	3.22	3.46							

The results highlighted in blue, which is 13mm of Al 7075 T6 combined with 2mm of SiC, represents the most lightweight configuration, tipping the scale at 3.22 kg. This configuration matches the performance of the 10mm Weldox 460E plate. Subsequently, a ballistic curve was graphed for this specific combination, involving a range of projectile initial velocities spanning from 161.2 m/s to 296 m/s.

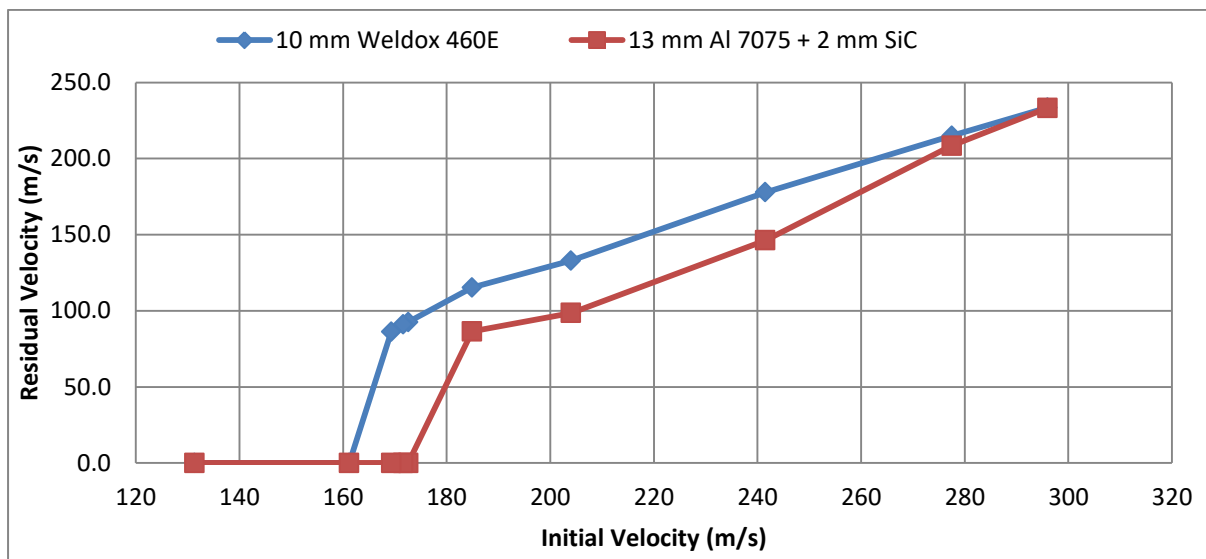


**Figure 6-11: Ballistic Curve for Combination of 13mm Al 7075 T6 and 2mm SiC**

This graph demonstrates that the selected multilayered target performs notably better at velocities below 240 m/s, resulting in substantially lower residual velocities when compared to the 10mm monolithic target. However, at an initial velocity of 296 m/s, both targets yield nearly identical residual velocities.

This curve provides evidence that the combination of 13mm Al 7075 T6 and 2mm SiC surpasses or equals the performance of the 10mm Weldox 460E across all initial velocities. Additionally, this combination boasts a weight of 3.22 kg, rendering it 2.69 kg lighter than the 5.89 kg weight of the 10mm Weldox 460E plate. It's noteworthy that this configuration is

also 1.04 kg lighter than the optimal Weldox 460E and SiC combination. However, its total thickness stands at 15mm, which is 6mm greater than the total thickness of the Weldox 460E – SiC combination that totals 9mm.

### 6.2.3 Weldox 460E – Al 7075 T6

The same study was undertaken for the combination of Weldox 460E and Al 7075 T6. The results were gathered through alterations in thickness, ranging from 1mm to 9mm, for both Weldox 460E and Al 7075 T6. In this setup, the Al 7075 T6 plate was positioned as the front layer, while the Weldox 460E plate was placed as the back layer, with no gap between them.

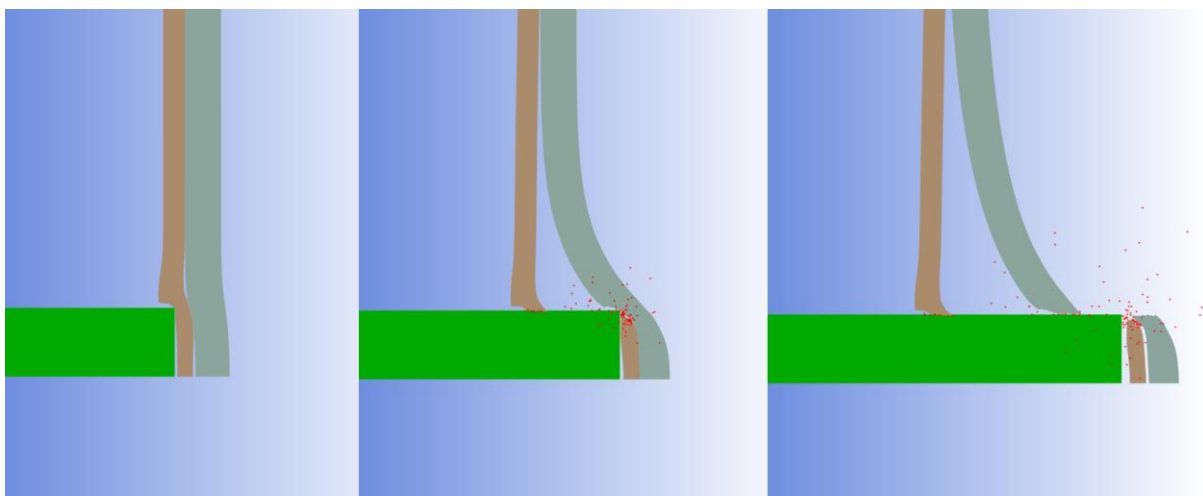


**Figure 6-12: Penetration in Weldox 460E - Al 7075 T6, Initial Velocity = 296m/s**

The initial velocity was set to 296 m/s. As shown in the figure above, Al 7075 T6 fails due to high shear stress and a plug shears off and pushes the back plate which also fails through plugging. The subsequent table provides the residual velocities for different configurations:

**Table 6-6: Residual Velocity for Varying Thickness of Weldox 460E - Al 7075 T6, Initial Velocity = 296m/s**

W460 E	Al 7075 T6								
	1 mm	2 mm	3 mm	4 mm	5 mm	6 mm	7 mm	8 mm	9 mm
1 mm									256.7
2 mm								245.6	
3 mm						247.1	237.2		
4 mm			242.6	240.1	235.4	230.0			
5 mm		243.9	224.5	217.8	206.0				
6 mm		229.7	220.4	202.9					
7 mm	245.2	220.9	204.9						
8 mm	222.2	209.1							
9 mm	216.1								

The results highlighted in green signify values below 233.49 m/s. Data was also collected for an initial velocity of 161.2 m/s. Among all the combinations marked in green in the previous table, the residual velocity measured 0 m/s when the initial velocity was set at 161.2 m/s. The subsequent table presents the weights in kilograms (kg) for various configurations. The density of Wieldox 460E is 7850 kg/m<sup>3</sup>, while the density of Al 7075 T6 stands at 2804 kg/m<sup>3</sup>.

**Table 6-7: Weight (kg) for Varying Thickness of Wieldox 460E - Al 7075 T6**

W460 E	Al 7075 T6								
	1 mm	2 mm	3 mm	4 mm	5 mm	6 mm	7 mm	8 mm	9 mm
1 mm									2.48
2 mm								2.86	
3 mm						3.03	3.24		
4 mm			2.99	3.20	3.41	3.62			
5 mm		3.36	3.57	3.78	4.00				
6 mm		3.95	4.16	4.37					
7 mm	4.33	4.54	4.75						
8 mm	4.92	5.13							
9 mm	5.51								

The result highlighted in blue, comprising 5mm of Wieldox 460E and 3mm of Al 7075 T6, represents the most lightweight configuration, with a weight of 3.57 kg. This setup achieves performance parity with the 10mm Wieldox 460E plate. Following this, a ballistic curve was graphed for this specific combination, encompassing a range of projectile initial velocities spanning from 161.2 m/s to 296 m/s.

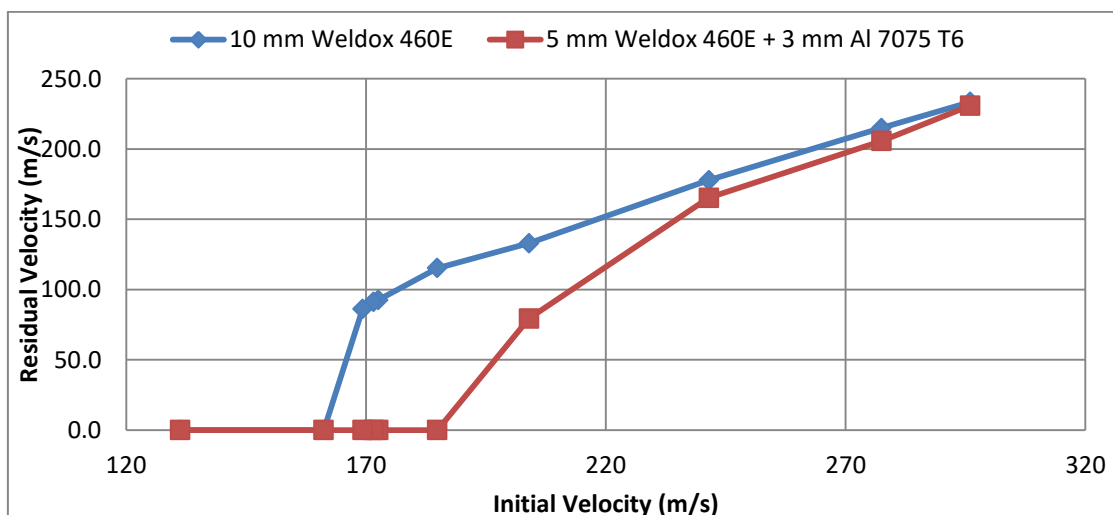


**Figure 6-13: Ballistic Curve for Combination of 5mm Wieldox 460E and 3mm Al 7075 T6**

This graph illustrates that the selected multilayered target exhibits superior performance at velocities below 240 m/s, leading to substantially lower residual velocities in comparison to

the 10mm monolithic target. However, with increasing velocity, the results gradually converge, and at an initial velocity of 296 m/s, both targets yield nearly identical residual velocities. This curve provides compelling evidence that the combination of 5mm Weldox 460E and 3mm Al 7075 T6 surpasses or equals the performance of the 10mm Weldox 460E across all initial velocities. Furthermore, this combination carries a weight of 3.57 kg, making it 2.32 kg lighter than the 5.89 kg weight of the 10mm Weldox 460E plate. This particular configuration, weighing 3.57 kg, is also 0.69 kg lighter than the Weldox 460E – SiC combination at 4.26 kg, but 0.35 kg heavier than the Al 7075 T6 – SiC combination at 3.22 kg.

Finally the following table shows the weight and total thickness of all the best combinations of different materials that were identified in this research compared to 10mm Weldox 460E.

**Table 6-8: Comparison of Different Target Configurations**

Sr. No.	Target Configurations	Thickness (mm)	Weight (kg)	Total Thickness (mm)
1	Weldox 460E	10	5.89	10
2	Weldox 460E - SiC	6,3	4.26	9
3	Al 7075 T6 - SiC	13,2	3.22	15
4	Weldox 460E - Al 7075 T6	5,3	3.57	8

Al 7075 T6 - SiC is the lightest combination 3.22 kg but with largest thickness 15mm. The combination of Weldox 460E – Al 7075 T6 is has the smallest thickness 8mm and has a slightly larger weight 3.57 kg than Al 7075 T6 – SiC. The combination Weldox 460E – SiC is the heaviest 4.26 kg compared to others with a thickness of 9 mm but it is still lighter nad thinner than 10 mm weldox 460E monolithic plate. If thickness is not a consideration than Al 7075 T6 – SiC is the best option but if thickness is considered Weldox 460E – Al 7075 T6 is the best combination among all the test configurations.

### 6.3 Results Discussion:

The results presented in this text show the outcomes of a study aimed at optimizing multi-layered target configurations for ballistic performance while minimizing weight. Three different material combinations were tested, and their respective findings are summarized below:

Weldox 460E – SiC: SiC ceramic, known for its low density, high compressive strength, and exceptional hardness, was paired with Weldox 460E. The objective was to match the

performance of a 10mm monolithic Weldox 460E plate while reducing weight. The best-performing configuration was 6mm Weldox 460E paired with 3mm SiC. This combination weighed 4.26 kg and outperformed the 10mm Weldox 460E plate at all initial velocities below 296 m/s. The reduction in weight by 3.26 kg was considered significant, especially for extended wear.

Al 7075 T6 – SiC: Similar to the first combination, this setup involved SiC paired with Al 7075 T6. The most effective configuration was found to be 13mm Al 7075 T6 combined with 2mm SiC, weighing 3.22 kg. This combination matched the performance of the 10mm Weldox 460E plate across various initial velocities. Although it was lighter, it had a larger thickness of 15mm compared to other configurations.

Weldox 460E – Al 7075 T6: This combination reversed the order, with Al 7075 T6 as the front layer and Weldox 460E as the back layer. The best configuration was 5mm Weldox 460E combined with 3mm Al 7075 T6, weighing 3.57 kg. This combination performed on par with the 10mm Weldox 460E plate at all initial velocities below 296 m/s. It was lighter than the 10mm plate and also lighter than the Weldox 460E – SiC combination.

In summary, the results showed that each combination had its advantages. Al 7075 T6 - SiC was the lightest but had the highest thickness. Weldox 460E – Al 7075 T6 had a good compromise between thickness and weight. Weldox 460E – SiC was heavier but still thinner than the 10mm Weldox 460E plate. The choice of configuration would depend on specific requirements, with Al 7075 T6 - SiC being the lightest option, and Weldox 460E – Al 7075 T6 being the best choice if thickness was a consideration.



## **Chapter 7: CONCLUSION**

This thesis has explored the ballistic analysis of different materials through a comprehensive review of relevant literature and an in-depth analysis of numerical simulations, this study aimed to shed light on the best alternatives for Weldox 460E.

Weldox 460E has been used for armor for a long time due to its exceptional ballistic performance but because of its high density it is considerably heavy. Through the course of this study, various material combinations were identified that exhibit both reduced weight compared to Weldox 460E and similar performance. Notably, the Al 7075 T6 and SiC combination stands out as the lightest option, but with a comparatively greater thickness. On the contrary, the pairing of Weldox 460E with SiC, although lighter than monolithic Weldox 460E plate, resulted in a higher weight in comparison to other multilayered armor configurations. Remarkably, the combination of Weldox 460E and Al 7075 T6 emerges as the optimal middle ground, effectively balancing weight and thickness considerations.

The outcomes of this study hold significant implications for the armor industry. The insights gleaned herein have the potential to pave the way for the development of novel lightweight armors.

## **Chapter 8: FUTURE WORK**

To assess the effectiveness of a ballistic-resistant shield, it must undergo testing against a variety of projectiles traveling at different velocities. This necessitates extensive experimental efforts, which, in turn, demand sophisticated equipment and setups to accurately measure impact and residual velocities. Finite Element Method (FEM) simulations offer the potential to minimize the reliance on empirical experimentation. Currently, Lagrangian-based codes provide reasonably comparable outcomes for cases involving moderate deformation. For situations involving significant deformations, mesh-free techniques like Smoothed Particle Hydrodynamics (SPH) or a hybrid approach combining FEM and SPH can be explored. SPH can be employed in regions of critical impact, complemented by FEM in the broader field. Further research could extend this work to predict the perforation behavior of a 7.62 mm projectile against various target configurations.

## REFERENCES

- [1] Jonas A. Zukas. “High Velocity Impact Dynamics”
- [2] T. Borvik et al. “Ballistic penetration and perforation of steel plates-an experimental and numerical investigation” *Advances in Dynamics and Impact Mechanics-2000*
- [3] T. Borvik et al. “Effect of target thickness in blunt projectile penetration of Weldox 460 E steel plates” *International Journal of Impact Engineering* 28 (2003) 413–464
- [4] Backman ME, Goldsmith W. “The mechanics of penetration of projectiles into targets” *International Journal of Engineering Sciences* 1987;16:1–99.
- [5] Yellup J. M. and R. L. Woodward, “Some investigation into the prevention of adiabatic shear failure in high strength armor materials” (1980) *Res. Mech.* pp 41-57
- [6] I. Marom and S. R. Bodner “Projectile perforation of multilayered beams” *International Journal of Mechanical Sciences*, 21(8):489 - 504, 1979.
- [7] J. Radin and W. Goldsmith. Normal projectile penetration and perforation of layered targets. *International Journal of Impact Engineering*, 7(2):229-259, 1988.
- [8] Curran et al. “Dynamic Failure in Solids” *Physics Today*” *Physics Today*, 30, 46-55, 1977
- [9] A. A. Almohandes, M. S. Abdel-Kader, and A. M. Eleiche. “Experimental investigation of the ballistic resistance of steel-fibreglass reinforced polyester laminated plates” *Composites Part B-Engineering*, 27(5):447-458, 1996.
- [10] S. Dey et al. “On the ballistic resistance of double-layered steel plates: An experimental and numerical investigation” 2006
- [11] V. S. Deshpande and N. A. Fleck, “One-Dimensional Response of Sandwich Plates to underwater Shock Loading,” *J.Mech. Phys. Solids*, 2347–83 (2005).
- [12] K. Nixdorff et al. “Application of the penetration theory of J. Awerbuch and S. R. Bodner on multilayered targets”, *Math. Mech.* 64:4 (1984), T147–T149.
- [13] J. W. Hutchinson and Z. Xue, “Metal Sandwich Plates Optimized for Pressure Impulses,” *Int. J. Mech. Sci.*, 545–69 (2005).
- [14] Madhu et al. 2003 V. Madhu, T. B. Bhat, and N. K. Gupta, “Normal and oblique impacts of hard projectiles on single and layered plates: An experimental study”, *Def. Sci. J.* 53:2 (2003), 147–156.
- [15] J. A. Zukas and D. R. Scheffler, “Impact effects in multilayered plates”, *Int. J. Solids Struct.* 38:19 (2001), 3321–3328.

- [16] Ben-Dor et al. 1998a] G. Ben-Dor, A. Dubinsky, and T. Elperin, “Effect of air gaps on ballistic resistance of targets for conical impactors”, *Theor. Appl. Fract. Mech.* 30:3 (1998), 243–249.
- [17] Ben-Dor et al. 1998b] G. Ben-Dor, A. Dubinsky, and T. Elperin, “On the ballistic resistance of multi-layered targets with air gaps”, *Int. J. Solids Struct.* 35:23 (1998).
- [18] G. Ben-Dor., A. Dubinsky, and T. Elperin, “Effect of air gap and order of plates on ballistic resistance of two layered armor”, *Theor. Appl. Fract. Mech.* 31:3 (1999), 233–241.
- [19] 19. Ben-Dor. et al. “The optimum arrangement of the plates in a multilayered shield”, *Int. J. Solids Struct.* 37:4 (2000), 687–696.
- [20] Ben-Dor. et al. 2005 “Ballistic impact: Recent advances in analytical modeling of plate penetration dynamics”, *Appl. Mech. Rev.* 58:6 (2005), 355–371. A review.
- [21] Ben-Dor. et al. “Applied high-speed plate penetration dynamics, Solid State and its Applications 132, Springer, Dordrecht, 2006.
- [22] Ben-Dor. et al., “Effect of air gaps on ballistic resistance of ductile shields perforated by non-conical impactors”, *J. Mech. Mater. Struct.* 1 (2006), 279–299.
- [23] Ben-Dor. et al., “Applied High Speed Plate Penetration Dynamics” 2006
- [24] Christian J. Yungwirth et al., “Explorations of Hybrid Sandwich Panel Concepts for Projectile Impact Mitigation” *J. Am. Ceram. Soc.*, S62–S75 (2011)
- [25] D.S. Preece, V.S. Berg, “Bullet impact on steel and Kevlar/steel armor-Computer modeling and experimental data” *Proceedings of ASME symposium, July 25-29, 2004*
- [26] S. Swaddiwudhipong et al. “High Velocity Penetration/Perforation Using Coupled Smooth Particle Hydrodynamics-Finite Element Method” *International Journal of Protective Structures – Volume 1 · Number 4 · 2010*
- [27] Jonas A. Zukas et al., “Practical Aspects of Numerical Simulations of Dynamic Events: Effects of Meshing” *International Journal of Impact Engineering-2000*
- [28] T.J. Holmquist and G.R. Johnson, “Determination of constants and comparison of results for various constitutive models” *Journal De Physique III, Vol. 1, Oct. 1991, pp. 853-860.*
- [29] Stefan Hiermaier, “Structures under Crash and Impact-Continuum Mechanics, Discretization and Experimental Characterization” Edition-2007.
- [30] Charles E. Anderson Jr. “A review of Computational ceramic Armor Modelling” *Advances in Ceramic Armor-II*

- [31] Yueming Liang et al. “Design and Simulation of Ballistic resistant Metal/Ceramic sandwich structures” *Advances in Ceramic Armor-2005*, pp 35-42.
- [32] Chen, X. W., and Li, Q. M., 2003, “Perforation of a Thick Plate by Rigid Projectiles,” *Int. J. Impact Eng*, pp. 743–759.
- [33] Johnson, W., “Impact Strength of Materials” London, Arnold, 1972 [pp. 342, 360, 361,366].
- [34] P. Lundberg et al. “Impact of conical tungsten projectiles on flat Silicon carbide targets: Transition from interface defeat to penetration” *Int. J. of Impact Engineering* 28 (2006) pp:1842-1856
- [35] T. Borvik et al. “Perforation of 12 mm thick steel plates by 20 mm Diameter projectiles with flat hemispherical and conical noses” *Int. J. of Impact Engineering* 2002;27(1):19 35.
- [36] ANSYS Help Manual
- [37] Dey S., High strength steel plates subjected to projectile impact – An experimental and numerical study” *Doctoral Thesis, Norwegian University of Science and Technology*, 2004
- [38] Forrestal M. J. et al. “Penetration of 6061 T651 aluminium targets with rigid long rods” *Journal of Applied Mechanics* 1988, 55, 755-760
- [39] Ravid M. et al. “Dynamic perforation of viscoplastic plates by rigid projectiles” *International Journal of Engineering Science* 1983, 21, 577-591
- [40] Borvik et al. “Numerical simulation of plugging failure in Ballistic penetration” *International Journal of Solid structures* 2001, 38, 6241-64
- [41] Chen et al. “On perforation of ductile metallic plates by blunt rigid projectile” *European Journal of Mechanics A/Solids* 2009, 28,273-283
- [42] Ahmad Serjoui et al. “An empirical model for ballistic limit of bi-layer ceramic/metal armour” *Procedia Engineering* 75 (2014) 14-18
- [43] Vitman at al. “ A simple method of determining the dynamical hardness of metals using a double cone” *Zavodskaja Laboratorjia* 14(6), 727-732
- [44] Guodong Guo at al. “Numerical analysis of ballistic impact performance of two ceramic-based armor structures” *Composites Part C*, (2020), 2666-6820
- [45] Yahui Shi at al. “Experimental and Numerical Study on the Protective Behavior of Weldox 900 E Steel Plates Impacted by Blunt-Nosed Projectiles” *Metals* (2022), 12, 141.